

# Drivetrain simulation using variational autoencoders

Pallavi Sharma<sup>1,2,3</sup>, Jorge-Humberto Urrea-Quintero<sup>4</sup>, Bogdan Bogdan<sup>1</sup>, Adrian-Dumitru Ciotea<sup>1</sup>, Laura Vasilie<sup>1</sup>, Henning Wessels<sup>4</sup> and Matteo Skull<sup>1</sup>

<sup>1</sup>Porsche Engineering, Etzelstraße 1, Bietigheim-Bissingen, 74321, Germany.

<sup>2</sup>Graduate Program Computational Sciences in Engineering, Technische Universität Braunschweig, Braunschweig, Germany.

<sup>3</sup>Fraunhofer Institute for Energy Economics and Energy System Technology, Joseph-Beuys-Straße 8, Kassel, 34117, Germany.

<sup>4</sup>Institute of Applied Mechanics, Division Data-Driven Modeling of Mechanical Systems, Technische Universität Braunschweig, Pockelsstraße 3, Braunschweig, 38106, Germany.

**Keywords:** generative AI, variational auto-encoders, latent space interpretation, drivetrain simulation, electric vehicles

## Abstract

This work proposes variational autoencoders (VAEs) to predict a vehicle's jerk signals from torque demand in the context of limited real-world drivetrain datasets. We implement both unconditional and conditional VAEs, trained on experimental data from two variants of a fully electric SUV with differing torque and drivetrain configurations. The VAEs synthesize jerk signals that capture characteristics from multiple drivetrain scenarios by leveraging the learned latent space. A performance comparison with baseline physics-based and hybrid models confirms the effectiveness of the VAEs, without requiring detailed system parametrization. Unconditional VAEs generate realistic jerk signals without prior system knowledge, while conditional VAEs enable the generation of signals tailored to specific torque inputs. This approach reduces the dependence on costly and time-intensive real-world experiments and extensive manual modeling. The results support the integration of generative models such as VAEs into drivetrain simulation pipelines, both for data augmentation and for efficient exploration of complex operational scenarios, with the potential to streamline validation and accelerate vehicle development.

## 1. Introduction

In automotive engineering, engineers must rely on datasets to accurately parameterize and validate the generalization capabilities of drivetrain simulation models. Ideally, these datasets should cover the variance of drivetrain hardware characteristics across the vehicle fleet and the broad variety of driving situations. However, the issue is that measurement collection in the real world can be very expensive [1]. Consequently, simulation engineers often have to work with sparse datasets that, for example, do not fully capture the variance in the jerk signal behavior across the vehicle fleet. A vehicle's drivetrain encompasses the components that deliver power from the engine/motor to the wheels, while jerk refers to the rate of change of acceleration, a key factor in perceived ride comfort. Vehicles with different mileage or drivetrain components with slightly different clearances can exhibit significant differences in their jerk behavior. A sparse or poorly distributed dataset, therefore, limits the generalization ability of a drivetrain model.

To mitigate this issue, synthetic measurements can be generated using non-generative methods that rely on models and their corresponding inputs to simulate new signals of interest [2]. Such a supervised approach to data augmentation can be greatly limited if the required input data for a physics-based or data-driven model are missing in the recorded measurement files or cannot be measured at all [3]. Another major drawback of this conventional approach is that it requires drivetrain engineers to deeply understand the underlying physical phenomena to determine which input data are necessary for a non-generative model to simulate additional valuable signals [4]. Furthermore, the more physically relevant

input information is fed into the model for precise simulation results, the more accurate the simulation will likely be. This input-output imbalance necessitates a large number of input parameters (like torque and speed of the electric machine) to simulate a single particular output, such as vehicle acceleration.

These limitations can be tackled with approaches from generative artificial intelligence (AI) [5, 6]. One such family of deep generative models includes unconditional architectures such as Variational Autoencoders (VAEs) [7, 8], which can be trained to generate new signals solely from a limited amount of available signals collected from physics-based, simulations, or a real system and does not require additional parametrization with respect to the system configuration. This self-supervised approach to data augmentation is purely data-driven. It eliminates the need for detailed domain expertise regarding the underlying physical principles of drivetrain simulation. While unconditional data augmentation can be highly advantageous for drivetrain engineers, it is also important to consider the value of conditional AI, for example, conditional VAEs (CVAEs) [9, 10, 11]. In this case, the generation of synthetic data is additionally conditioned on other inputs, similar to supervised data augmentation. This can significantly minimize the need for real-world on-road testing, making generative AI a powerful tool for addressing incomplete datasets.

The black-box nature of generative models could lead to poor acceptance among drivetrain experts if the generated signals cannot be explained and validated from an engineering perspective. Therefore, a key aspect of using generative AI, in particular VAEs, in the context of drivetrain simulation is the analysis and interpretation of the information encoded in the latent space [12, 13, 14]. This interpretation step ensures the generation of new signals that are physically plausible. It also helps identify regions in the latent space that match specific simulation requirements, such as a particular driver torque demand. In this sense, the main contribution of this paper is to demonstrate that VAEs can serve as effective generative models for drivetrain simulation, bypassing the need for exhaustive manual system parametrization by interpreting the latent space or conditioning new data generation on specific desired features while maintaining physical plausibility.

The outline of this paper is as follows. First, we introduce the drivetrain simulation problem in Section 2 and explain the different possible approaches to address it. Second, we present the theoretical background for VAEs in Section 3 and extensions that yield conditional VAEs. Section 4 presents the dataset and the challenges it imposes for VAE training. We then train unconditional and conditional VAEs to address the problem of jerk signal generation and measure their performance using different metrics. We also compare the performance of the trained VAEs with respect to a physics-based and a hybrid model. The manuscript concludes in Section 5.

## 2. Drivetrain simulation problem

A key performance indicator for quantifying vehicle drivability is the jerk, defined as the rate of change of acceleration. During abrupt positive changes in acceleration, known as tip-in load changes, the torsion in the driveshaft fluctuates, stimulating vibrations in the natural frequency range of the drivetrain (0-2 Hz and 8-12 Hz) [15]. These longitudinal oscillations negatively affect vehicle dynamics, leading to reduced drivability performance and driver discomfort [15, 16]. Although this issue is present in vehicles with combustion engines, it becomes more pronounced in electric vehicles due to their higher torque gradients [17]. The primary control variable for managing the jerk is torque demand, although it is also influenced by drivetrain parameters such as gear ratio, vehicle mass, and tire dynamics. Furthermore, parameters such as electric machine (ELM) speed and road conditions—referred to as driving scenario parameters—significantly impact jerk behavior.

Simulation of vehicle drivability under varying driving scenarios can drastically improve drivetrain development efficiency by reducing the reliance on physical road tests, saving both time and resources [18]. Several models exist to simulate the effects of drivetrain and driving scenarios on jerk behavior [19, 20, 21, 22]. These models typically predict the jerk as a function of the torque demand. In this context, sudden pedal pressure (tip-in) or release (tip-out) are key driving events. Drivetrain models

can generally be categorized into physics-based, data-driven, and hybrid models.

**Physics-based models** have been the most widely used approach to simulate drivetrain oscillations in various driving scenarios and drivetrain configurations [19, 23]. For example, a simplified model of the drive axle of a battery electric vehicle often consists of two masses: the electric machine and the wheel, connected by a finitely rigid drive shaft modeled as a torsion spring [23, 24, 25]. Changes in torque demand, whether during acceleration or braking, alter the torsion in the shaft, exciting vibrations in the natural frequency range of the drivetrain.

These models are typically implemented in environments such as MATLAB/Simulink, as demonstrated, for example, in [26, 27, 28]. They are often integrated within Hardware-in-the-Loop (HIL) setups to simulate real-life driving conditions [18]. They include models of the whole transmission system, covering aspects like torque transmission and gear settings. Physics-based models are straightforward to implement and yield immediate results, making them reliable tools for drivetrain simulations.

However, the accuracy of these models comes at the cost of complexity. Detailed physics-based models, which have been iteratively refined by experts over time, require deep domain knowledge and significant experience. Although effective, these traditional models are not always suitable for the fast-paced and disruptive development cycles of modern electric vehicles, where rapid iteration and efficiency are critical [18].

With the rise of machine learning, particularly in supervised learning, **data-driven models** have gained prominence in drivetrain simulation [22, 21]. These models are often viewed as “black box” approaches, which is advantageous when the underlying physics are too complex to be modeled explicitly [22]. Typically, data-driven models are trained on annotated datasets where hardware parameters serve as input features and the measured acceleration is used as the target label. The resulting acceleration data is then transformed into jerk signals as required.

Data-driven approaches involve complex calculations and require large neural network architectures with numerous parameters, making them computationally intensive [29, 30, 31]. Other limitations are that neural networks are generally less interpretable than physics-based models, which limits their acceptance among simulation engineers. Moreover, these models often struggle with extrapolation [32], as they perform poorly outside the range of training data. To address this, some researchers have explored physics-informed neural networks [32, 33, 34, 35], which incorporate physical constraints into the machine learning model to improve performance and reliability.

**Hybrid models** combine the strengths of both data-driven and physics-based approaches [22, 36, 37, 38]. In the context of drivetrain simulation, they typically begin with a simplified physics-based model that captures the most critical physical phenomena. This ensures that the essential dynamics are grounded in physics. A data-driven correction term is added to account for any modeling discrepancies or to refine the model [39].

Hybrid models not only require a solid understanding of the underlying physics but are also input-intensive [39]. In addition to torque demand, several other control variables, such as hardware configurations and driving conditions, must be incorporated into the hybrid model. This comprehensive set of inputs is necessary for both the initial physical simulation and the subsequent data-driven correction, making these models highly versatile but computationally demanding.

In summary, the advent of battery electric vehicles has created a significant demand for more flexible, accurate, and efficient drivetrain modeling beyond state-of-the-art physics-based approaches. Although supervised data-driven and hybrid models offer good accuracy, they are often data-intensive, which limits their efficiency. To address this challenge, this work explores generative models, more precisely VAEs, as a promising solution to simulate drivetrain behavior, with the aim of balancing accuracy and resource efficiency.

### 3. Variational autoencoders as generative models for data augmentation

This section provides a theoretical foundation for the use of VAEs as generative models in the context of drivetrain simulations. First, we discuss the transformation of measured jerk signals into spectrograms in Section 3.1, which are used as input for the various VAE architectures. In Section 3.2, unconditional VAEs are introduced, focusing on their encoder-decoder structure, probabilistic latent space representation, and the objective function that drives their training. The concepts of CVAE and Gaussian mixture model (GMM)-CVAE are presented in Sections 3.3 and 3.4, respectively, explaining how conditioning on auxiliary variables and the use of mixture models in the latent space enhance flexibility and control over new spectrograms generation.

#### 3.1. Transformation between time domain jerk signal and spectrogram

The measurement data that we aim to augment in this study consists of time-domain jerk signals. Prior to their augmentation via the different VAE architectures considered, these signals are transformed into spectrograms, that is, represented in the frequency domain using a short-time Fourier transform (STFT) [40, 41]. After augmentation, the generated spectrograms are converted back into time-domain jerk signals using the inverse short-time Fourier transform (iSTFT). In this work, we rely on the PyTorch implementations for STFT and iSTFT [42].

Projecting time-domain signals into the spectral domain (spectrograms) was chosen as it offers several advantages for processing with VAEs, especially those utilizing convolutional neural network (CNN) encoders and decoders. Spectrograms provide a rich time-frequency representation, allowing the model to learn and capture localized temporal and spectral patterns simultaneously. This can be more effective than using raw time-series data, as CNNs can more readily extract relevant features from the 2D structure of a spectrogram, potentially simplifying the network architecture and improving the ability to model complex signal characteristics.

**Time domain jerk signal to spectrogram:** Let  $s(n)$  denote the discrete jerk signal, where  $n$  is the discrete time index. The transformation of the discrete-time signal  $s(n)$  to its spectrogram representation follows from

$$S(f, t) = \sum_{n=-\infty}^{\infty} s(n) w(t - n) e^{-j2\pi f n}, \quad (3.1)$$

where  $S(f, t)$  is the complex-valued STFT of the signal  $s(n)$ ,  $f$  represents the frequency,  $t$  represents the time position of the analysis window (in terms of discrete time steps), and  $w(t - n)$  is the window function (e.g., Hanning window) applied at time  $t$ . From  $S(f, t)$ , the magnitude  $|S(f, t)|$  and phase  $\varphi$  can be extracted as follows,

$$\begin{aligned} |S(f, t)| &= \sqrt{\operatorname{Re}(S(f, t))^2 + \operatorname{Im}(S(f, t))^2}, \\ \varphi(f, t) &= \arg(S(f, t)) = \tan^{-1} \left( \frac{\operatorname{Im}(S(f, t))}{\operatorname{Re}(S(f, t))} \right). \end{aligned} \quad (3.2)$$

where  $\operatorname{Re}(S(f, t))$  and  $\operatorname{Im}(S(f, t))$  are the real and imaginary parts of  $S(f, t)$ , respectively.

To compress the dynamic range of the magnitude spectrogram, a logarithmic scaling is applied,

$$x_{ft} = \log(|S(f, t)| + \epsilon), \quad (3.3)$$

where  $\epsilon$  is a small constant which prevents us from taking the logarithm of zero. The log-scaled magnitude spectrogram  $\mathbf{x} \in \mathbb{R}^{F \times T}$ , with frequency resolution  $f \in [0, F]$ , time resolution  $t \in [0, T]$ , and components  $x_{ft}$ , is used as input for the VAE architectures. In the following, for the sake of brevity, we will refer to the log-scaled magnitude of a spectrogram simply as the spectrogram  $\mathbf{x}$ .

This logarithmic scaling is a common practice in signal processing as it helps to enhance the details of lower-energy components in the spectrogram and makes the distribution of the input features more suitable for neural network training by preventing high-magnitude values from disproportionately influencing the learning process. For jerk signals, oscillations at lower frequencies can be particularly important for drivability perception, and log-scaling can aid in better representing these nuances.

**Spectrogram to time domain jerk signal:** In the interest of as-compact-as-possible VAE architectures, herein, we only augment the magnitude of the spectrogram, while the phase is estimated in a post-processing step after augmentation. This approach simplifies the design of the neural networks for the encoder and decoder in the VAEs, as reconstructing both the magnitude and phase simultaneously within the same network can be challenging. Additionally, the phase of jerk signals typically exhibits minimal variation, further justifying this simplification. Thus, when the VAE is used as a generative model, the phase  $\varphi$  is unknown and is estimated using the Griffin-Lim algorithm [40].

That is, given a generated log-scaled magnitude spectrogram  $\mathbf{x}$  and estimated phase  $\hat{\varphi}$ , first, we recover the non-log-scaled magnitude spectrogram as

$$|\hat{S}(f, t)| = \exp(\mathbf{x}) - \epsilon. \quad (3.4)$$

Then, the discrete jerk signal  $\hat{s}(n)$  is reconstructed from the magnitude and phase using the iSTFT.

### 3.2. Variational Autoencoder (VAE)

Generative models aim to learn the underlying probability distribution of observed data  $\mathbf{x}$ , enabling density estimation and the generation of new samples that resemble the original data or its reconstruction [43]. The VAE is a generative model first introduced in [9] that learns a lower-dimensional latent representation  $\mathbf{z}$  to capture the essential features and structure of high-dimensional input data in a compressed way [44], which in the current context are spectrograms  $\mathbf{x}$  as introduced in the above Section 3.1.

The hidden random generative process of  $\mathbf{x}$  consists of two steps: First, the latent variable  $\mathbf{z}$  is sampled from some prior distribution  $p(\mathbf{z})$ . This prior  $p(\mathbf{z})$  is chosen to be a standard Gaussian distribution,  $p(\mathbf{z}) = \mathcal{N}(\mathbf{z} \mid \mathbf{0}, \mathbf{I})$ , where  $\mathbf{I}$  is the identity matrix. This choice simplifies calculations, particularly for the regularization term in the objective function, and encourages a well-behaved latent space. Thus,  $\mathbf{z} \sim p(\mathbf{z})$ . Second, a value  $\mathbf{x}$  is generated by some conditional distribution  $p_{\theta}(\mathbf{x} \mid \mathbf{z})$ , i.e.  $\mathbf{x} \sim p_{\theta}(\mathbf{x} \mid \mathbf{z})$ . We aim to find  $p_{\theta}(\mathbf{x} \mid \mathbf{z})$  (the parameters  $\theta$ ), such that we can sample from  $p(\mathbf{z})$  and with high probability,  $\mathbf{x} \sim p_{\theta}(\mathbf{x} \mid \mathbf{z})$  follows the same distribution as the  $\mathbf{x}$  in our dataset [9]. From a mathematical point of view, this can be achieved by maximizing the marginal log-likelihood of  $\mathbf{x}$  (also termed the log evidence). The marginal log-likelihood is expressed as:

$$\log p_{\theta}(\mathbf{x}) = \log \int p_{\theta}(\mathbf{x}, \mathbf{z}) d\mathbf{z} = \log \int p_{\theta}(\mathbf{x} \mid \mathbf{z}) p(\mathbf{z}) d\mathbf{z}. \quad (3.5)$$

Here,  $p_{\theta}(\mathbf{x} \mid \mathbf{z})$  represents the likelihood of observing data  $\mathbf{x}$  given latent variables  $\mathbf{z}$  and model parameters  $\theta$ , while  $p(\mathbf{z})$  is the prior over  $\mathbf{z}$ . Maximizing  $\log p_{\theta}(\mathbf{x})$  with respect to  $\theta$  inherently optimizes the parameters of the likelihood function  $p_{\theta}(\mathbf{x} \mid \mathbf{z})$ . This is because, to render the observed data  $\mathbf{x}$  maximally probable under the integral, the likelihood  $p_{\theta}(\mathbf{x} \mid \mathbf{z})$  must assign high probabilities to  $\mathbf{x}$  for latent variables  $\mathbf{z}$  that are themselves likely under the prior  $p(\mathbf{z})$ . Thus, this process compels the model to learn a likelihood function that effectively explains the generation of the observed data. This marginal likelihood  $p_{\theta}(\mathbf{x})$  is challenging to compute because:

- The latent variable  $\mathbf{z}$  may be high-dimensional, making Monte Carlo-based integration over  $\mathbf{z}$  practically infeasible.
- While the likelihood  $p_{\theta}(\mathbf{x} \mid \mathbf{z})$  (parameterized by the decoder) is typically tractable for a given  $\mathbf{z}$ , the integration  $\int p(\mathbf{z}) p_{\theta}(\mathbf{x} \mid \mathbf{z}) d\mathbf{z}$  for computing the marginal likelihood  $p_{\theta}(\mathbf{x})$  is often intractable,

especially when  $p_\theta(\mathbf{x} | \mathbf{z})$  is a complex function (e.g., a deep neural network) or when no closed-form solution for the integral exists.

Therefore, it was suggested in [9] to compute  $\log p_\theta(\mathbf{x})$  in terms of the expectation  $\mathbb{E}_{p_\theta(\mathbf{z}|\mathbf{x})}[\bullet] = \int p_\theta(\mathbf{z} | \mathbf{x})(\bullet) d\mathbf{z}$  w.r.t. the posterior  $p_\theta(\mathbf{z} | \mathbf{x})$  such that,

$$\log p_\theta(\mathbf{x}) = \log \mathbb{E}_{p_\theta(\mathbf{z}|\mathbf{x})} \left[ \frac{p_\theta(\mathbf{x}, \mathbf{z})}{p_\theta(\mathbf{z} | \mathbf{x})} \right]. \quad (3.6)$$

The issue is that as  $p_\theta(\mathbf{x})$  is intractable,  $p_\theta(\mathbf{z} | \mathbf{x})$  is also intractable. Therefore, to approximate the intractable posterior  $p_\theta(\mathbf{z} | \mathbf{x})$ , a variational distribution  $q_\phi(\mathbf{z} | \mathbf{x})$  is introduced, parameterized by  $\phi$  (e.g., through a neural network). The goal will be to make  $q_\phi(\mathbf{z} | \mathbf{x})$  as close as possible to  $p_\theta(\mathbf{z} | \mathbf{x})$ , i.e.,  $q_\phi(\mathbf{z} | \mathbf{x}) \approx p_\theta(\mathbf{z} | \mathbf{x})$ . In VAEs, the posterior  $q_\phi(\mathbf{z} | \mathbf{x})$  and the likelihood  $p_\theta(\mathbf{x} | \mathbf{z})$  are implemented as neural networks: the encoder and decoder, respectively.

**Encoder:** It approximates the (untractable) posterior  $p_\theta(\mathbf{z} | \mathbf{x})$  with a variational distribution  $q_\phi(\mathbf{z} | \mathbf{x})$ , typically chosen as a Gaussian  $\mathcal{N}$  with a diagonal covariance matrix,

$$q_\phi(\mathbf{z} | \mathbf{x}) = \mathcal{N}(\mathbf{z} | \mu_\phi(\mathbf{x}), \text{diag}(\sigma_\phi^2(\mathbf{x}))). \quad (3.7)$$

Here,  $\mu_\phi(\mathbf{x}) \in \mathbb{R}^{n_z}$  and  $\sigma_\phi(\mathbf{x}) \in \mathbb{R}^{n_z}$  are the mean and standard deviation, respectively (with  $n_z$  the dimension of the latent space), and are obtained from

$$(\mu_\phi(\mathbf{x}), \sigma_\phi(\mathbf{x})) = \text{NN}_{\text{enc}}(\mathbf{x}; \phi), \quad (3.8)$$

where  $\text{NN}_{\text{enc}}$  is the encoder neural network parametrized in  $\phi$ , that branches into the two outputs  $(\mu_\phi(\mathbf{x}), \sigma_\phi(\mathbf{x}))$ . The parameter set  $\phi$  includes all weights and biases necessary to produce both  $\mu_\phi(\mathbf{x})$  and  $\sigma_\phi(\mathbf{x})$ . The encoder bridges the data space and the latent space.

**Decoder:** It approximates the likelihood  $p_\theta(\mathbf{x} | \mathbf{z})$  with a neural network  $\text{NN}_{\text{dec}}(\mathbf{z}; \theta)$ , parameterized by  $\theta$ , to output the mean of a Gaussian distribution

$$p_\theta(\mathbf{x} | \mathbf{z}) = \mathcal{N}(\mathbf{x} | \text{NN}_{\text{dec}}(\mathbf{z}; \theta), \text{diag}(\lambda^2)), \quad (3.9)$$

where  $\lambda \in \mathbb{R}^{F \times T}$  is a vector that defines the scale of the output covariance. In practice,  $\lambda$  can either be fixed (e.g.,  $\lambda = \lambda \mathbf{1}$  for some scalar  $\lambda > 0$ ), or learned as part of the model, depending on the modeling assumptions. In this study, we set  $\lambda$  to a constant value of 1.0 for all output dimensions. This choice makes the negative log-likelihood reconstruction term in the ELBO (Equation 3.17) equivalent to a scaled Mean Squared Error plus a constant, a common practice that encourages the decoder to learn the mean of the data distribution effectively. While more complex output distributions are possible, this choice provides a balance between model expressiveness and computational tractability for many types of continuous data. Notice that during training, the decoder takes latent variables  $\mathbf{z}$  sampled from the approximate posterior  $q_\phi(\mathbf{z} | \mathbf{x})$  and learns to approximate the likelihood  $p_\theta(\mathbf{x} | \mathbf{z})$ . During generation, it takes  $\mathbf{z}$  sampled from the prior  $p(\mathbf{z})$  and generates new samples  $\mathbf{x}$ . That is, the decoder bridges the latent space and the data space.

**Objective Function:** Coming back to Equation (3.6) and using the definition of the joint probability in terms of the posterior, that is,  $p(\mathbf{x}, \mathbf{z}) = p(\mathbf{z} | \mathbf{x}) p(\mathbf{x})$ , it follows that,

$$\log p_\theta(\mathbf{x}) = \mathbb{E}_{q_\phi(\mathbf{z}|\mathbf{x})} \left[ \log \frac{p_\theta(\mathbf{x}, \mathbf{z})}{q_\phi(\mathbf{z} | \mathbf{x})} \right] + \mathbb{E}_{q_\phi(\mathbf{z}|\mathbf{x})} \left[ \log \frac{q_\phi(\mathbf{z} | \mathbf{x})}{p_\theta(\mathbf{z} | \mathbf{x})} \right]. \quad (3.10)$$

The second term is the Kullback-Leibler (KL) divergence between  $q_\phi(\mathbf{z} | \mathbf{x})$  and  $p_\theta(\mathbf{z} | \mathbf{x})$ :

$$D_{\text{KL}}(q_\phi(\mathbf{z} | \mathbf{x}) \| p_\theta(\mathbf{z} | \mathbf{x})) = \mathbb{E}_{q_\phi(\mathbf{z}|\mathbf{x})} \left[ \log \frac{q_\phi(\mathbf{z} | \mathbf{x})}{p_\theta(\mathbf{z} | \mathbf{x})} \right]. \quad (3.11)$$

However, since the KL divergence is always greater or equal to zero by definition, it can be neglected and the remaining first term is known as the *Evidence Lower Bound* (ELBO):

$$\mathcal{L}_{\theta, \phi}(\mathbf{x}) = \mathbb{E}_{q_{\phi}(\mathbf{z}|\mathbf{x})} [\log p_{\theta}(\mathbf{x}, \mathbf{z}) - \log q_{\phi}(\mathbf{z}|\mathbf{x})]. \quad (3.12)$$

Therefore, Equation (3.10) can be rewritten as,

$$\begin{aligned} \log p_{\theta}(\mathbf{x}) &\geq \mathbb{E}_{q_{\phi}(\mathbf{z}|\mathbf{x})} \left[ \log \frac{p_{\theta}(\mathbf{x}, \mathbf{z})}{q_{\phi}(\mathbf{z}|\mathbf{x})} \right], \\ &\geq \mathcal{L}_{\theta, \phi}(\mathbf{x}). \end{aligned} \quad (3.13)$$

Maximizing the marginal log-likelihood is, therefore, equivalent to maximizing the ELBO. Moreover, to maximize the ELBO, we can equivalently minimize its negative. The negative ELBO is used as the VAE loss function:

$$\{\phi^*, \theta^*\} = \arg \min_{\phi, \theta} -\mathcal{L}_{\theta, \phi}(\mathbf{x}). \quad (3.14)$$

Substituting the joint distribution  $p_{\theta}(\mathbf{x}, \mathbf{z}) = p(\mathbf{z}) p_{\theta}(\mathbf{x}|\mathbf{z})$  into the ELBO, Equation (3.12), yields,

$$\mathcal{L}_{\theta, \phi}(\mathbf{x}) = \mathbb{E}_{q_{\phi}(\mathbf{z}|\mathbf{x})} [\log p_{\theta}(\mathbf{x}|\mathbf{z})] + \mathbb{E}_{q_{\phi}(\mathbf{z}|\mathbf{x})} [\log p(\mathbf{z}) - \log q_{\phi}(\mathbf{z}|\mathbf{x})]. \quad (3.15)$$

The second term in the above equation can again be rewritten as a KL divergence. Thus, the ELBO becomes:

$$\mathcal{L}_{\theta, \phi}(\mathbf{x}) = \mathbb{E}_{q_{\phi}(\mathbf{z}|\mathbf{x})} [\log p_{\theta}(\mathbf{x}|\mathbf{z})] - D_{\text{KL}}(q_{\phi}(\mathbf{z}|\mathbf{x})\|p(\mathbf{z})), \quad (3.16)$$

where:

- The first term,  $\mathbb{E}_{q_{\phi}(\mathbf{z}|\mathbf{x})} [\log p_{\theta}(\mathbf{x}|\mathbf{z})]$ , is the **reconstruction error term**. It measures how well the decoder  $p_{\theta}(\mathbf{x}|\mathbf{z})$  can reconstruct the original data  $\mathbf{x}$  from the latent variable  $\mathbf{z}$ .
- The second term,  $D_{\text{KL}}(q_{\phi}(\mathbf{z}|\mathbf{x})\|p(\mathbf{z}))$ , is the **regularization error term**, which ensures that the approximate posterior  $q_{\phi}(\mathbf{z}|\mathbf{x})$  is close to the prior  $p(\mathbf{z})$ .

Thus, the ELBO given by Equation (3.16) is computationally feasible and serves as a surrogate for the initial objective function in Equation (3.10). Expanding the terms, the VAE loss function in Equation (3.14) becomes:

$$-\mathcal{L}_{\theta, \phi}(\mathbf{x}) = \underbrace{\mathbb{E}_{q_{\phi}(\mathbf{z}|\mathbf{x})} [-\log p_{\theta}(\mathbf{x}|\mathbf{z})]}_{\text{Reconstruction Loss}} + \underbrace{D_{\text{KL}}(q_{\phi}(\mathbf{z}|\mathbf{x})\|p(\mathbf{z}))}_{\text{Regularization Loss}}. \quad (3.17)$$

So far, we presented the derivation of the objective function assuming  $\mathbf{x}$  to be one datapoint (one spectrogram) in our dataset, i.e.,  $\mathbf{x} = \mathbf{x}^{(i)}$ , where our whole dataset is  $\mathbf{X} = \{\mathbf{x}^{(i)}\}_{i=1}^{n_d}$  (with  $n_d$  the number of spectrograms in the dataset). Consequently, given the multiple spectrograms  $\mathbf{x}^{(i)}$  in the dataset, we need to construct an estimator of the marginal likelihood lower bound of the full dataset as

$$-\mathcal{L}_{\theta, \phi}(\mathbf{X}) = -\sum_{i=1}^{n_s} \mathcal{L}_{\theta, \phi}(\mathbf{x}^{(i)}). \quad (3.18)$$

By minimizing this loss function (3.18) for the neural network parameters  $\phi$  and  $\theta$ , the VAE learns both a probabilistic latent representation  $\mathbf{z}$  of the data  $\mathbf{x}$  and a generative model capable of reconstructing or sampling new data points  $\mathbf{x}$ . This approach leads to latent spaces that are well-structured, continuous, and, in some cases, interpretable.

**Reparameterization Trick:** To enable gradient-based optimization through stochastic sampling, the VAE employs the reparameterization trick. Instead of sampling  $\mathbf{z}$  directly from  $\mathcal{N}(\boldsymbol{\mu}_\phi(\mathbf{x}), \text{diag}(\boldsymbol{\sigma}_\phi^2(\mathbf{x})))$ , we consider

$$\mathbf{z} = \boldsymbol{\mu}_\phi(\mathbf{x}) + \boldsymbol{\sigma}_\phi(\mathbf{x}) \odot \boldsymbol{\epsilon}, \quad (3.19)$$

where  $\boldsymbol{\epsilon} \sim \mathcal{N}(\mathbf{0}, \mathbf{I})$  is an auxiliary noise variable, and  $\odot$  denotes element-wise multiplication. This formulation isolates the randomness in  $\boldsymbol{\epsilon}$ , allowing gradients to flow through  $\boldsymbol{\mu}_\phi(\mathbf{x})$  and  $\boldsymbol{\sigma}_\phi(\mathbf{x})$ .

### 3.3. Conditional Variational Autoencoder (CVAE)

Conditional VAE (CVAE) extends standard (unconditional) VAE by conditioning the encoder and decoder on additional information, such as class labels or auxiliary data [9, 44, 45]. In this case, the observed data  $\mathbf{x}$  is generated from a conditional likelihood distribution  $p_\theta(\mathbf{x} | \mathbf{z}, \mathbf{c})$ , parameterized by  $\theta$ , i.e.,  $\mathbf{x} \sim p_\theta(\mathbf{x} | \mathbf{z}, \mathbf{c})$ . The goal is to learn the parameters  $\theta$  of the conditional likelihood  $p_\theta(\mathbf{x} | \mathbf{z}, \mathbf{c})$  such that, by sampling  $\mathbf{z} \sim p(\mathbf{z})$  and conditioning on  $\mathbf{c}$ , the generated samples  $\mathbf{x} \sim p_\theta(\mathbf{x} | \mathbf{z}, \mathbf{c})$  resemble the data distribution of  $\mathbf{x}$  in the dataset for the given condition  $\mathbf{c} \in \mathbb{R}^{n_c}$  (with  $n_c$  the number of conditions).

From a mathematical perspective, this can be achieved by maximizing the marginal log-likelihood of  $\mathbf{x}$ , conditioned on  $\mathbf{c}$ ,

$$\log p_\theta(\mathbf{x} | \mathbf{c}) = \log \int p_\theta(\mathbf{x}, \mathbf{z} | \mathbf{c}) d\mathbf{z} = \log \int p(\mathbf{z}) p_\theta(\mathbf{x} | \mathbf{z}, \mathbf{c}) d\mathbf{z}. \quad (3.20)$$

As with the unconditional VAE, computing the marginal likelihood  $p_\theta(\mathbf{x} | \mathbf{c})$  is challenging. To address this challenge, the posterior distribution  $p_\theta(\mathbf{z} | \mathbf{x}, \mathbf{c})$  is approximated by a variational distribution  $q_\phi(\mathbf{z} | \mathbf{x}, \mathbf{c})$ , parameterized by  $\phi$  (e.g., through an encoder network).

The conditional information is integrated into the encoder-decoder as follows:

1. The posterior from Equation (3.7) becomes

$$q_\phi(\mathbf{z} | \mathbf{x}, \mathbf{c}) = \mathcal{N}(\mathbf{z} | \boldsymbol{\mu}_\phi(\mathbf{x}, \mathbf{c}), \text{diag}(\boldsymbol{\sigma}_\phi^2(\mathbf{x}, \mathbf{c}))), \quad (3.21)$$

and the **encoder** defined in Equation (3.8) modifies to

$$\text{NN}_{\text{enc}}(\mathbf{x}, \mathbf{c}; \phi) = (\boldsymbol{\mu}_\phi(\mathbf{x}, \mathbf{c}), \text{diag}(\boldsymbol{\sigma}_\phi^2(\mathbf{x}, \mathbf{c}))). \quad (3.22)$$

2. The **decoder** takes  $(\mathbf{z}, \mathbf{c})$  to generate  $\mathbf{x}$ , and the likelihood becomes

$$p_\theta(\mathbf{x} | \mathbf{z}, \mathbf{c}) = \mathcal{N}(\mathbf{x} | \text{NN}_{\text{dec}}(\mathbf{z}, \mathbf{c}; \theta), \text{diag}(\lambda^2)). \quad (3.23)$$

3. The **objective function** from Equation (3.17) is modified to account for the condition  $\mathbf{c}$  as follows,

$$-\mathcal{L}_{\theta, \phi}^{\text{CVAE}}(\mathbf{x}) = \mathbb{E}_{q_\phi(\mathbf{z} | \mathbf{x}, \mathbf{c})} \left[ -\log p_\theta(\mathbf{x} | \mathbf{z}, \mathbf{c}) \right] + D_{\text{KL}}(q_\phi(\mathbf{z} | \mathbf{x}, \mathbf{c}) \| p(\mathbf{z})). \quad (3.24)$$

In the context of this paper, CVAEs will allow the generation of new driving scenarios under specific conditions  $\mathbf{c}$ , performing the same task as simulator models or traditional simulation methods. This conditioning is achieved by incorporating torque demand as the conditioning variable in CVAEs during training.

### 3.4. Gaussian Mixture Model Conditional Variational Autoencoder (GMM-CVAE)

The GMM-CVAE further extends the standard VAE by modeling the latent space using a mixture of Gaussian distributions instead of a single Gaussian [11]. In this approach, the latent space  $\mathbf{z}$  is modeled

as a mixture of  $K$  Gaussian components, which defines the prior on the latent space, that is,

$$p(\mathbf{z}) = \sum_{k=1}^K \pi_k \mathcal{N}(\mathbf{z} \mid \boldsymbol{\mu}_k, \boldsymbol{\Sigma}_k). \quad (3.25)$$

Here,  $\pi_k$  represents the mixture weights, where  $\sum_{k=1}^K \pi_k = 1$ , and  $\boldsymbol{\mu}_k, \boldsymbol{\Sigma}_k$  are the mean and covariance of the  $k$ -th Gaussian component. The mixture weights  $\pi_k$  represent the prior probability of each Gaussian component. They encode global information about how the data is distributed across the latent space. For instance, if one component corresponds to a cluster of data with higher frequency,  $\pi_k$  determines its relative importance in the mixture.

During training, the encoder network  $\text{NN}_{enc}(\mathbf{x}, \mathbf{c}; \boldsymbol{\phi})$  learns the conditioned mean and covariance  $(\boldsymbol{\mu}_{\boldsymbol{\phi},k}(\mathbf{x}, \mathbf{c}), \boldsymbol{\Sigma}_{\boldsymbol{\phi},k}(\mathbf{x}, \mathbf{c}))$  of the variational posterior  $q_{\boldsymbol{\phi}}(\mathbf{z} \mid \mathbf{x}, \mathbf{c})$ , which is defined as,

$$q_{\boldsymbol{\phi}}(\mathbf{z} \mid \mathbf{x}, \mathbf{c}) = \sum_{k=1}^K \gamma_k(\mathbf{x}, \mathbf{c}) \mathcal{N}(\mathbf{z} \mid \boldsymbol{\mu}_{\boldsymbol{\phi},k}(\mathbf{x}, \mathbf{c}), \boldsymbol{\Sigma}_{\boldsymbol{\phi},k}(\mathbf{x}, \mathbf{c})). \quad (3.26)$$

The mixture weights  $\gamma_k(\mathbf{x}, \mathbf{c})$ , which represent the responsibility of the  $k$ -th component for the data point  $\mathbf{x}$ , are computed as

$$\gamma_k(\mathbf{x}, \mathbf{c}) = \frac{\pi_k \mathcal{N}(\mathbf{z} \mid \boldsymbol{\mu}_{\boldsymbol{\phi},k}(\mathbf{x}, \mathbf{c}), \boldsymbol{\Sigma}_{\boldsymbol{\phi},k}(\mathbf{x}, \mathbf{c}))}{\sum_{j=1}^K \pi_j \mathcal{N}(\mathbf{z} \mid \boldsymbol{\mu}_{\boldsymbol{\phi},j}(\mathbf{x}, \mathbf{c}), \boldsymbol{\Sigma}_{\boldsymbol{\phi},j}(\mathbf{x}, \mathbf{c}))}. \quad (3.27)$$

Here, the notation  $\mathcal{N}(\mathbf{z} \mid \boldsymbol{\mu}, \boldsymbol{\Sigma})$  refers to the probability density function of the Gaussian distribution evaluated at a sample  $\mathbf{z}$ . The responsibilities  $\gamma_k(\mathbf{x}, \mathbf{c})$  effectively denote the posterior probability of the latent variable  $\mathbf{z}$  (associated with input  $\mathbf{x}$  under condition  $\mathbf{c}$ ) belonging to the  $k$ -th Gaussian component of the mixture. During training, to sample from  $q_{\boldsymbol{\phi}}(\mathbf{z} \mid \mathbf{x}, \mathbf{c})$ , a component  $k$  is typically chosen according to these responsibilities (interpreted as  $P(k \mid \mathbf{x}, \mathbf{c})$ ), and then  $\mathbf{z}$  is sampled from  $\mathcal{N}(\mathbf{z} \mid \boldsymbol{\mu}_{\boldsymbol{\phi},k}(\mathbf{x}, \mathbf{c}), \boldsymbol{\Sigma}_{\boldsymbol{\phi},k}(\mathbf{x}, \mathbf{c}))$ .

Notice that the responsibilities  $\gamma_k(\mathbf{x}, \mathbf{c})$  depend on  $\pi_k$ , as the posterior distribution is a push-forward of the prior for specific input data. The term  $\pi_k$  scales the contribution of each Gaussian component in the posterior. This ensures that the posterior aligns with both the global prior (encoded by  $\pi_k$ ) and the specific data point  $\mathbf{x}$ . By combining the prior  $p(\mathbf{z})$  with the learned variational posterior  $q_{\boldsymbol{\phi}}(\mathbf{z} \mid \mathbf{x}, \mathbf{c})$ , the GMM-CVAE effectively models latent distributions and captures multimodal or clustered data structures.

The objective for the GMM-CVAE remains the same as in Equation (3.24), but  $q_{\boldsymbol{\phi}}(\mathbf{z} \mid \mathbf{x}, \mathbf{c})$  is now defined as in Equation (3.26) to include the mixture of Gaussians in the KL divergence.

## 4. Numerical results

In this section, we present the results obtained for the various VAE models introduced in Section 3. First, we provide an overview of the dataset used to train the VAE models in Section 4.1. Next, we study the performance of the VAE models in Section 4.2, focusing on their ability to accurately reproduce the spectrograms. Sections 4.2.1 and 4.2.2 analyze the unconditional and conditional VAE, respectively. We analyze the latent space learned by the VAEs and demonstrate the generation of new jerk signals by sampling from this latent space. The performance of the VAE, CVAE, and GMM-CVAE is quantitatively evaluated using several metrics. These metrics are computed to assess the quality of reconstruction and generative ability of the models. A comparison between the three models is made based on the computed metrics. Section 4.3 compares the predictive performance of a physics-based drivetrain (hardware) model, a hybrid model, and the CVAE generative model.

#### 4.1. Data acquisition and preproscessing

**Data acquisition:** In this work, we rely on a dataset that contains measurements of two variants of a fully electric SUV, which mainly differ in the maximum torque delivery of their electric machines and the number of driven wheels (4-wheel drive vs. 2-wheel drive). The dataset contains 636 vehicle's acceleration time signals, whose temporal derivative is the jerk.

The tests were performed on a powertrain test bench equipped with electric machines, each connected to one axle of the drivetrain hardware. This setup allows for easy programming of a series of positive (tip-in) and negative (tip-out) torque gradient steps, enabling precise measurement of the resulting acceleration. The primary advantage of this experimental setup is that it allows us to generate these torque changes exactly at the desired operating points and accurately reproduce them when swapping the drivetrain hardware with that of another vehicle or when testing different driving modes, such as Normal and Sport.

Figure 1 shows the distribution of the experimental jerk signals, that is, torque values  $M$  against the electric machine speed  $v$  at which the jerk signal (represented by a point) was collected. The torque is within the interval  $M \in [-250, 1000]$  Nm, and the electric machine speed  $v \in [0, 14000]$  rpm. The signals were recorded for a duration of 20 seconds. Upon recording the data, the signal is divided into short time-frame windows, each of 60 milliseconds, consisting of one jerk signal per time-frame window. This is done to capture each jerk signal separately to perform STFT, as defined in Equation (3.1), on each signal waveform.

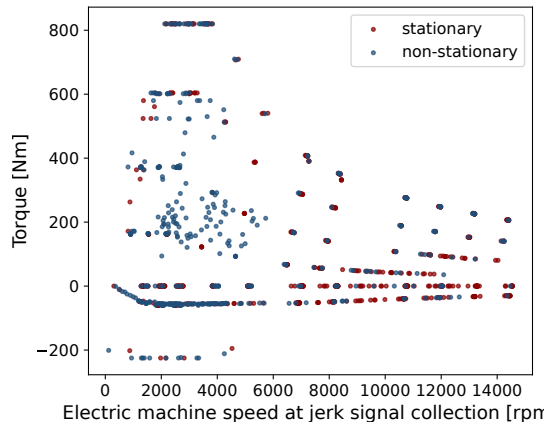


Figure 1: **Distribution of the available experimental jerk signal-data:** Torque vs. electric machine speed at which the jerk signal (represented by a point) was collected. Only the stationary measurements derived from these signals were considered for VAE training. Notice that the observed non-uniformity in the sampling reflects the inherent distribution within the collected measurement campaign, not a specific sampling choice for this visualization.

**Stationarity:** It is important to verify the stationarity of the jerk signals in the time domain prior to computing its Fourier transform, which in turn is used to compute the spectrograms. Moreover, since we are constrained to a relatively large FFT window size (32 samples) for the spectrogram due to frequency resolution constraints, it is more important to consider a stationarity test. A stationary signal refers to a time signal whose statistical properties, such as mean, variance, and autocorrelation, do not change over time, making it easier to model. Statistical stationarity tests such as Augmented Dickey-Fuller (ADF) [46] and Kwiatkowski-Phillips-Schmidt-Shin (KPSS) [47] can be applied to identify the presence of non-stationarity in the jerk signals. In this work, ADF test is performed using the statsmodels library in Python [48].

Figure 2 illustrates that 320 jerk signals (around 51%) lie in the ideal region, fulfilling the  $p$ -value criteria for the ADF test. Hence, these 320 jerk signals can be called stationary in time and converted into spectrograms to be used as input to the VAE model.

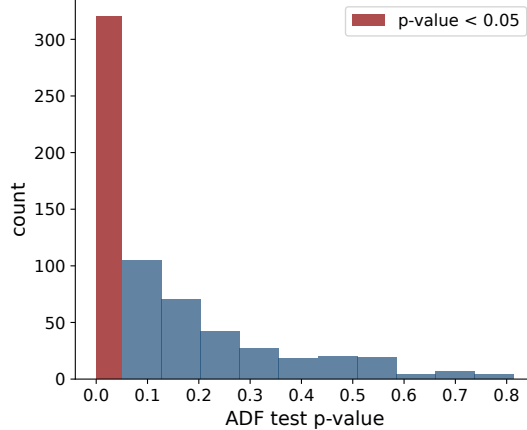


Figure 2: **Stability analysis:** ADF stationarity test showing that 320 jerk signals fulfill the  $p$ -value criteria ( $p < 0.05$ ) and can be considered stationary.

**Signal transformation:** We compute the corresponding spectrograms for the remaining  $n_s = 320$  stationary jerk signals using STFT as explained in Section 3.1. Table 1 lists the hyperparameters and their respective values for the STFT.

parameters	value
Hop Size	2 samples
Window	Hanning Window
Window Size	32 samples
Total Signal Length	60 samples
sampling frequency	50 Hz

Table 1: **STFT hyperparameters:** list of the parameters required to perform STFT used in this work to obtain the spectrograms from the jerk signals.

Figure 3 shows the result of transformation for one arbitrarily chosen signal, where Figure 3a is the jerk time-signal waveform and Figure 3b its corresponding spectrogram for the magnitude part. Note that the logarithmic scaling applied to the spectrogram compresses its amplitude values, making the amplitude unitless. Therefore, no units are displayed in the colorbar legend. The resulting 320 spectrograms of dimension  $17 \times 39$  pixels are used as input to the VAEs considered in the present work. Data normalization and splitting of the dataset into a train, validation, and test set in the ratio 0.7:0.2:0.1, respectively, are performed as a final preprocessing step before training the VAEs.

The reader should notice that the time-domain signals and their corresponding spectrograms may exhibit a discrepancy in their time axes. This is due to the nature of the STFT. The spectrogram represents overlapping windowed segments of the signal, where the time resolution depends on the hop size and window function specified in Table 1. A small hop size, in this case 2, results in a higher number of time frames, stretching the spectrogram along the time axis. This discrepancy

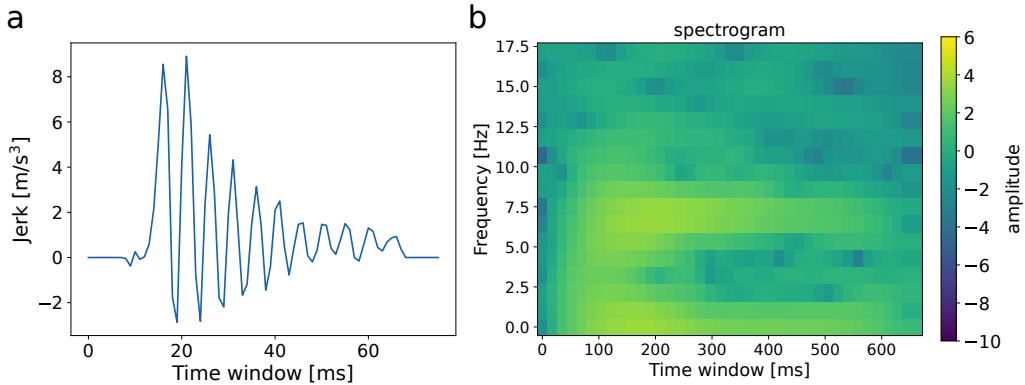


Figure 3: **Signal transformation:** **a** Jerk signal and **b** spectrogram obtained from STFT.

is a consequence of time-frequency analysis and does not indicate a misalignment in data representation.

**Spectrograms characterization:** We analyze the characteristics of the spectrograms to understand challenges for VAE training by assessing the distribution of pixel values and Signal-to-Noise Ratio (SNR). The pixel values, which represent the amplitude in the frequency domain, range from approximately -10.33 to 3.39, with a standard deviation of 1.005 (Figure 3b). These values indicate a significant dynamic range, with the data spread over a wide interval. The SNR of the original data is around 5.5 dB, which suggests that the signals contain substantial noise, as evidenced by abrupt changes in magnitude reflected in the contrast between light and dark pixel regions. As a result, any model trained on this data must be capable of accounting for noise while preserving the underlying structure of the spectrograms. These metrics highlight the core challenge of training a VAE for the drivetrain simulation task: the data contains noise, and any successful model must balance noise reduction on the one hand and maintain the essential features of the spectrograms on the other.

#### 4.2. Variational autoencoders as generative models for data augmentation

We present the numerical results for the different variants of VAEs introduced in Section 3. All VAEs have been implemented in Python using the PyTorch library [42]. In each variant, the VAE architecture consists of an encoder and a decoder, both implemented using convolutional neural networks (CNNs). The encoder comprises four convolutional layers with increasing channel sizes of 32, 64, 96, and 128, each using a kernel size of 3 and padding set to ‘same’. Notice that in the context of VAEs, the channel size of a convolutional layer denotes the number of feature maps it produces. Increasing the number of channels in successive layers allows the network to capture more complex and abstract features. Additionally, setting padding to ‘same’ ensures that the output height and width are the same as the input dimensions. This is achieved by adding an appropriate amount of zero-padding around the input so that the convolutional operation does not reduce the spatial size. Each convolutional layer is followed by a ReLU activation function, batch normalization, and a max pooling layer with a stride of 2, effectively reducing the spatial dimensions. After the convolutional blocks, the feature maps are flattened and passed through three linear layers, each mapping from 256 input features to a latent dimension of 64, to produce the latent representation, that is, mean and variance. The decoder mirrors the encoder structure by first mapping the latent vector back to a higher-dimensional space through a linear layer, followed by an unflattening operation. It then employs a series of upsampling layers with scale factors of 2 and convolutional layers that progressively reduce the channel dimensions from 128 to 1. Specifically, the decoder includes convolutional layers with 96, 64, 32, and finally 1 output channel, using kernel sizes of 1 and 3 with ‘same’ padding. A single output channel means that each pixel (or point) represents

a single value, in this case, the log-scale spectrogram magnitude  $x_{ft}$  from Equation (3.3). Activation functions between layers are primarily ReLU, except for the final output layer, which produces the reconstructed input without activation. This symmetric encoder-decoder framework enables the VAE to learn the latent representations for generating and reconstructing the spectrograms.

In the case of CVAE, additional conditioning information, in this case the torque demand, is introduced by concatenating the conditioning vector with the input of the encoder and decoder.

An empirical hyperparameter search was conducted to optimize the model architecture (including aspects like the number of layers, filter sizes, and latent dimension) and the training process (such as learning rate and choice of optimizer). This involved iterative experimentation and evaluation on a validation set, guided by common practices in VAE applications. Details regarding the final architecture and selected hyperparameters can be found in Table 2.

hyperparameters	value
epochs	300
learning Rate	0.0001
optimizer	Adam
NN layers in encoder-decoder	5
latent vector dimension	64

Table 2: **VAE hyperparameters:** Table listing the hyperparameters obtained for training the VAE, CVAE and GMM-CVAE architectures.

#### 4.2.1. Unconditional VAE

In this subsection, we focus on the unconditional VAE as introduced in Section 3.2.

**Performance evaluation:** The values obtained for each quantitative metric defined in Appendix A to measure the VAE’s performance are summarized in Table 3. These metrics were obtained using the test data. From the metrics, the unconditional VAE demonstrates reasonable reconstruction ability given the noisy nature of the input data. The Mean Squared Error (MSE) and Mean Absolute Error (MAE) are 0.3551 and 0.4203, respectively. These values suggest that the reconstructed spectrograms are generally close to the original ones but with some deviations. The normalized MSE and MAE, which account for the natural variability in the data, slightly adjust to 0.3577 and 0.2969, indicating that the VAE effectively captures key data patterns despite the noise.

Structural similarity is measured using the Structural Similarity Index Measure (SSIM), which is 0.6082, showing moderate structural alignment between the original and reconstructed spectrograms. This suggests that while the VAE captures the general structure of the data, some finer details may be lost or smoothed out. The Peak Signal-to-Noise Ratio (PSNR), at approximately 16.7421 dB for the unconditional VAE, reflects the balance between noise reduction and data fidelity in the reconstructed spectrograms. While this PSNR value might be considered moderate in some image reconstruction tasks, it is important to interpret it in the context of VAEs and the nature of our data. VAEs are designed to learn a compressed and regularized latent representation, which often results in a smoothing or denoising effect on the reconstructions, particularly for inherently noisy input data (our original spectrograms have an SNR of about 5.5 dB). This smoothing can result in the loss of some fine-grained details or noise present in the original, thereby reducing the PSNR. This is a consequence of the model prioritizing a generalizable latent space and capturing the underlying data structure over achieving perfect pixel-wise reconstruction. Lastly, the model’s SNR output of 9.6040 dB indicates an improvement over the original data’s SNR, suggesting the VAE does achieve some denoising while preserving essential signal characteristics. Overall, the VAE successfully extracts core data patterns from the noisy spectrograms, providing accurate reconstructions without overly distorting the input.

Figure 4 exemplarily illustrates the performance of the unconditional VAE for a specific jerk signal. Figure 4a compares the original and generated jerk signals in the time domain, showing strong alignment, indicating good reconstruction capability. In Figure 4b, the original spectrogram is displayed, while Figure 4c shows the generated spectrogram of the VAE, which closely resembles the original. Figure 4d depicts the absolute error between the original and generated spectrograms. Local discrepancies, observed as pronounced peaks in the absolute error plot, can be attributed to noise in the original spectrograms. As characteristic of VAEs, particularly due to the regularization imposed by the KL divergence term and the bottleneck structure, the model tends to reconstruct a smoothed version of the input, effectively filtering some of the high-frequency noise. This behavior is evident in Figure 4c appearing less noisy than Figure 4b. These discrepancies and the loss of some noise components contribute to the reconstruction error but also highlight the VAE’s ability to capture the more salient underlying features. The average error remains relatively low (Table 3), suggesting that the VAE has effectively learned this underlying structure, providing a smooth yet robust reconstruction of the original jerk signal.

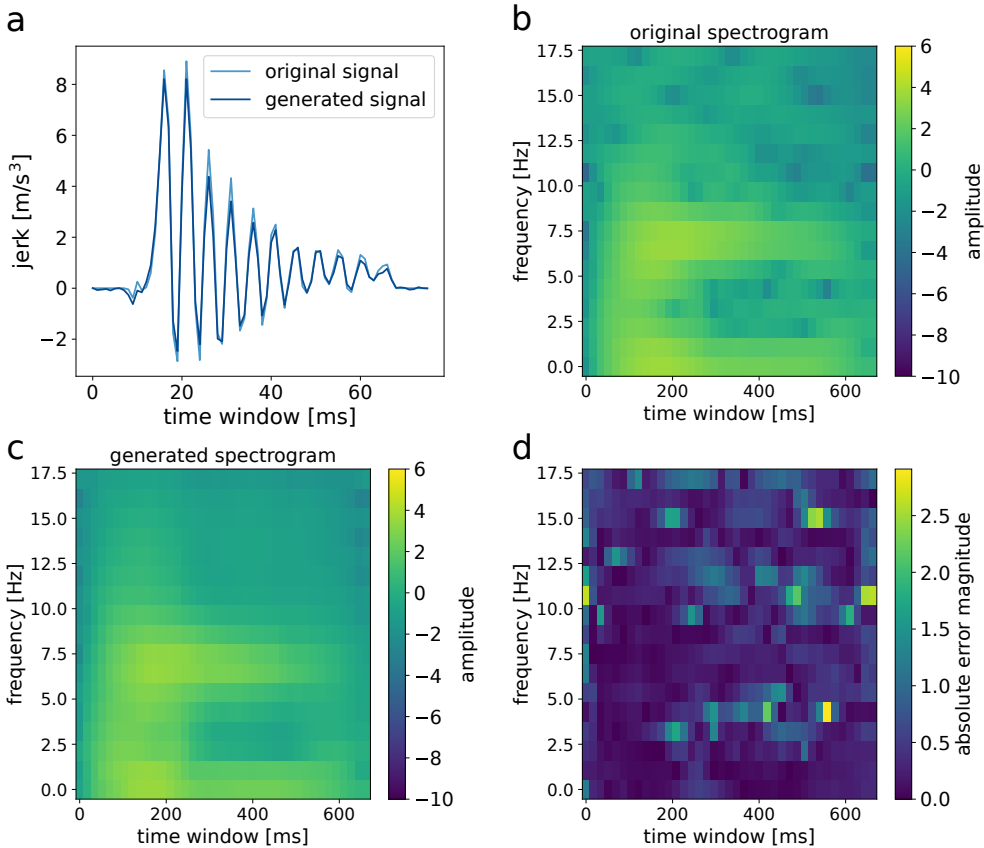
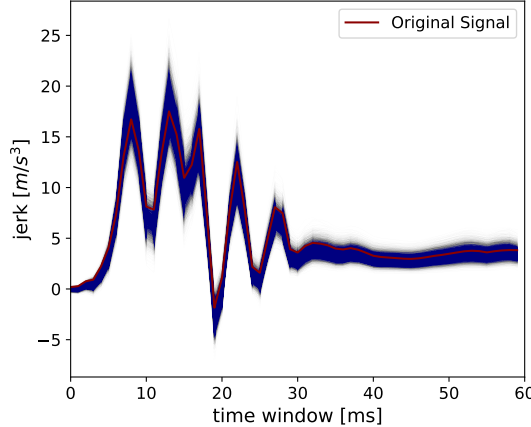


Figure 4: **VAE:** Model performance evaluation in reconstructing the original spectrogram and jerk signal. **a** comparison between the original and generated jerk signals in the time domain, **b** original spectrogram, **c** generated spectrogram from the VAE, and **d** absolute error between the original and generated spectrograms.

**Generation of new samples using the reparametrization trick:** For a given spectrogram  $\mathbf{x}$ , the latent mean ( $\mu_\phi(\mathbf{x})$ ) and variance ( $\sigma^2$ ) are computed using the encoder network from Equation (3.8). Making

use of the reparametrization trick from Equation 3.19, we sample the noise vector  $\epsilon \sim \mathcal{N}(\mathbf{0}, \mathbf{1})$  to obtain realizations of the latent variable  $\mathbf{z}$ . The VAE decodes each sample from the latent distribution into a jerk signal with statistical properties similar to the original.

Figure 5 displays 10,000 realizations of jerk signals. These signals are generated by first encoding the original jerk signal (red) to obtain its latent distribution  $q_\phi(\mathbf{z}|\mathbf{x}_{\text{original}})$ , then repeatedly sampling  $\mathbf{z}$  from this distribution using the reparameterization trick (Equation 3.19), and finally decoding these latent samples. The phase for all signals is estimated using the Griffin-Lim algorithm. The close alignment between the original jerk signal and the envelope of these generated signals demonstrates the VAE's ability to learn a consistent encoding and to represent local variability around a given input.



**Figure 5: Reparametrization trick - VAE generated jerk signal variability:** Comparison of the original jerk signal (red) with the mean (e.g., solid blue line) and standard deviation envelope (e.g., shaded blue region) of 10,000 jerk signals generated by sampling from the latent posterior  $q_\phi(\mathbf{z}|\mathbf{x}_{\text{original}})$  using the reparameterization trick (Equation 3.19) and then decoding. The decoder output variance  $\lambda$  is fixed (see Section 3.2), so the displayed variability originates from the latent space sampling.

**Latent space interpretation and generation of new jerk signals:** VAEs have an inherent limitation: they generate new outputs (spectrograms) that generally cannot be directly controlled on the basis of specific inputs (features). This drawback can be addressed by leveraging the VAE's latent space. For instance, t-Distributed Stochastic Neighbor Embedding (t-SNE) can be used to transform the 64-dimensional latent representations into a 2D space, making it interpretable through visualizations like scatter plots [49, 50]. Then, we can generate new spectrograms  $\mathbf{x}$  that reflect specific characteristics or patterns of the original data. A well-structured (or "well-distributed") latent space correlates directly with the generative capabilities of the VAE architecture. Such a latent space ideally exhibits desirable properties like continuity (whereby small changes in the latent vector lead to correspondingly small changes in the generated output), smoothness, and a meaningful organization where different data variations are encoded in a somewhat disentangled or structured manner. These characteristics are crucial for enabling robust interpolation between data points and controlled generation of novel samples. It influences the variety of features captured when sampling new data points and the overall quality and coherence of the generated data.

Particularly, in this work, we generate new spectrograms  $\mathbf{x}$  by sampling from a labeled reduced latent space as follows:

1. The set of original latent vectors  $\mathbf{Z}_{train} = \{\mathbf{z}^{(i)}\}_{i=1}^{N_{train}} \subset \mathbb{R}^{n_z}$  obtained by encoding the training dataset spectrograms is projected into a 2D space using the t-SNE algorithm:

$$\mathbf{Z}_{t\text{-SNE},train} = t\text{-SNE}(\mathbf{Z}_{train}), \quad (4.1)$$

where  $\mathbf{Z}_{t\text{-SNE},train} = \{\mathbf{z}_{t\text{-SNE}}^{(i)}\}_{i=1}^{N_{train}} \subset \mathbb{R}^2$ . This 2D embedding is used for visualization.

2. For a chosen pre-defined category of interest (e.g., a specific torque range), we identify the subset of training data points belonging to this category. Let this subset of 2D t-SNE embeddings be  $\mathbf{Z}'_{t\text{-SNE}} \subset \mathbf{Z}_{t\text{-SNE},train}$ . We then compute the empirical mean  $\mu'_{t\text{-SNE}}$  and covariance  $\Sigma'_{t\text{-SNE}}$  of the points in  $\mathbf{Z}'_{t\text{-SNE}}$ . New points in the 2D visualization space, denoted  $\mathbf{z}_{t\text{-SNE},new}$ , are sampled from a Gaussian distribution parameterized by these statistics:

$$\mathbf{z}_{t\text{-SNE},new} \sim \mathcal{N}(\mu'_{t\text{-SNE}}, \Sigma'_{t\text{-SNE}}). \quad (4.2)$$

3. To obtain a corresponding high-dimensional latent vector  $\mathbf{z}_{new} \in \mathbb{R}^{n_z}$  for each  $\mathbf{z}_{t\text{-SNE},new}$ , we employ the k-Nearest Neighbors (k-NN) algorithm available in the Python library scikit-learn [51, 52]. Specifically, for a given  $\mathbf{z}_{t\text{-SNE},new}$ , we identify the  $k$  training data points in  $\mathbf{Z}_{t\text{-SNE},train}$  that are closest (in Euclidean distance) to  $\mathbf{z}_{t\text{-SNE},new}$ . Let their corresponding original high-dimensional latent vectors be  $\{\mathbf{z}^{*(1)}, \dots, \mathbf{z}^{*(k)}\} \subset \mathbf{Z}_{train}$ . The new high-dimensional latent vector  $\mathbf{z}_{new}$  is then computed as a weighted average of these  $k$  neighbors:

$$\mathbf{z}_{new} = \sum_{j=1}^k w_j \mathbf{z}^{*(j)}, \quad \text{where } w_j = \frac{\exp(-d(\mathbf{z}_{t\text{-SNE},new}, \mathbf{z}_{t\text{-SNE}}^{(j)})/\tau)}{\sum_{l=1}^k \exp(-d(\mathbf{z}_{t\text{-SNE},new}, \mathbf{z}_{t\text{-SNE}}^{(l)})/\tau)}, \quad (4.3)$$

$d(\cdot, \cdot)$  is the Euclidean distance, and  $\tau$  is a parameter controlling the smoothness (larger  $\tau$ ) or sharpness (smaller  $\tau$ ) of the weighting distribution applied to the k-NN. In our implementation, we used  $k = 5$  and  $\tau = 0.1$ . This step aims to find a plausible point in the original latent space that is consistent with the location sampled in the 2D visualization.

4. Finally, a new spectrogram  $\mathbf{x}_{new}$  is generated by passing the derived high-dimensional latent vector  $\mathbf{z}_{new}$  through the VAE's decoder:

$$\mathbf{x}_{new} \sim p_{\theta}(\mathbf{x} \mid \mathbf{z}_{new}). \quad (4.4)$$

This procedure leverages the t-SNE visualization to identify regions associated with known physical characteristics (e.g., specific torque ranges). By sampling from these regions in the 2D t-SNE space and then mapping back to the original latent space, the aim is to generate new data that shares these desired physical attributes. However, it is important to acknowledge that t-SNE is a non-linear dimensionality reduction technique primarily designed for visualization, and it may not preserve the global structure of the data perfectly. Therefore, the process of sampling in the t-SNE space and then reconstructing to the original latent space is an exploratory method with inherent limitations regarding the precision of the inverse mapping. The resulting samples' appropriateness for the target physical category depends on how well the VAE's latent space is organized.

In this work, we use the t-SNE implementation from the Python library scikit-learn [52], which takes as input  $\mathbf{Z}$  and a scalar indicating the number of desired t-SNE components after dimensionality reduction and returns  $\mathbf{Z}_{t\text{-SNE}}$ , which is the projection of  $\mathbf{Z}$  onto the t-SNE components.

Figure 6 shows the latent space of the unconditional VAE model, obtained by mapping the 64-dimensional latent vectors  $\mathbf{Z}$  to a 2D representation  $\mathbf{Z}_{t\text{-SNE}}$  using t-SNE for visualization purposes. The data points in this 2D projection are colored and shaped (i.e., labeled) by the two vehicle types (Figure 6a) and seven torque ranges (Figure 6b), which are subsets of the interval  $[-300, 1000]$  Nm. A different marker shape represents each torque range, and ellipses are drawn around these predefined groups based on their covariance in the 2D t-SNE space to highlight their approximate distribution and separation. It

is observed that vehicle type better categorizes the data than torque range. However, lower (0 - 50 Nm) and higher (600 - 1000 Nm) torque categories show tighter clustering compared to other ranges, as seen by their compact ellipses. The other torque categories tend to overlap more, suggesting that the latent representations for these torque ranges may not be as easily distinguished from each other. This overlap is common when the VAE finds similarities in the latent features of different categories. Overall, the plot highlights the distribution and spread of the data in the latent space, and the presence of distinct clusters suggests that the VAE has learned meaningful latent features, particularly with respect to vehicle types.

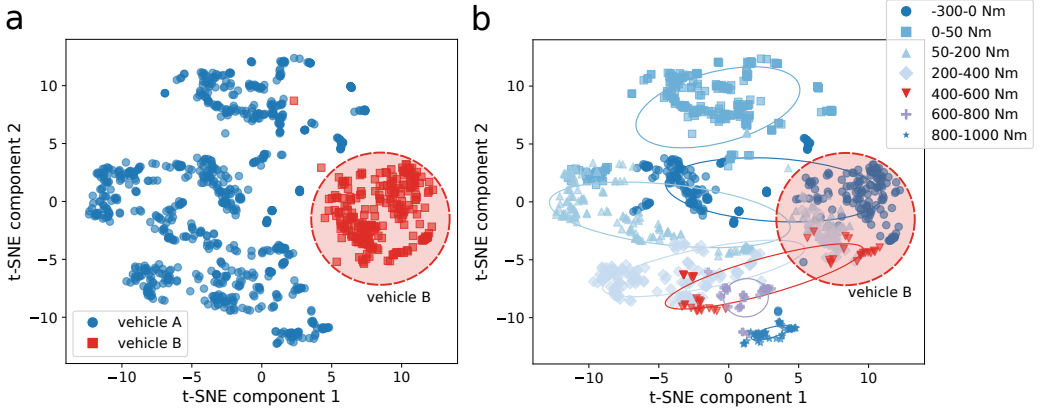


Figure 6: **Latent space interpretation and labeling:** Clusters are observed for **a** the two different vehicle types and **b** seven torque ranges.

Figure 7 shows jerk signals generated as explained above. Here, we sample within the torque clusters, but the reader should notice that the same can be done for the different types of vehicles or any other user-defined category. Each row in the figure corresponds to a specific torque range in the interval  $[-300, 1000]$  Nm, and consists of three subplots: **a** a generated spectrogram  $\mathbf{x}_k$  as well as the corresponding **b** jerk signal in the time domain and **c** the frequency spectrum.

The spectrograms in Figure 7a display frequency components over time for the generated jerk signals, demonstrating how the VAE can reconstruct plausible frequency representations. Figure 7b shows the jerk signals generated in the time domain, where variations in the torque range lead to different signal shapes. Figure 7c shows the frequency spectrum of each jerk signal. The jerk signals in the training and testing datasets used for VAE training consistently exhibit their highest amplitudes around 0-2 Hz and 8-12 Hz. Notice that these frequencies align with vibrations in the drivetrain's natural frequency range caused by abrupt acceleration changes. Therefore, we shaded the frequency bands (0-2 Hz and 8-12 Hz) to emphasize that the generated signals are physically plausible. Griffin-Lim algorithm [40] is applied here to estimate the phase (see Section 3.2) by starting with a random initialization and iteratively refining the phase estimate. An accurate estimation of the phase was achieved after 1,000 iterations, which took less than 1 second to complete.

#### 4.2.2. Conditional VAEs

This section discusses the results obtained using conditional VAEs, specifically CVAE and GMM-CVAE, using the same network hyperparameters specified in Table 2.

**Performance evaluation:** Table 3 compares the unconditional VAE, CVAE, and GMM-CVAE performance. The table reveals that the unconditional VAE consistently performs slightly better on most metrics when evaluated on spectrogram reconstruction. It achieves the lowest reconstruction errors (MSE = 0.3551, MAE = 0.4203), suggesting that it is more effective in accurately reconstructing noisy

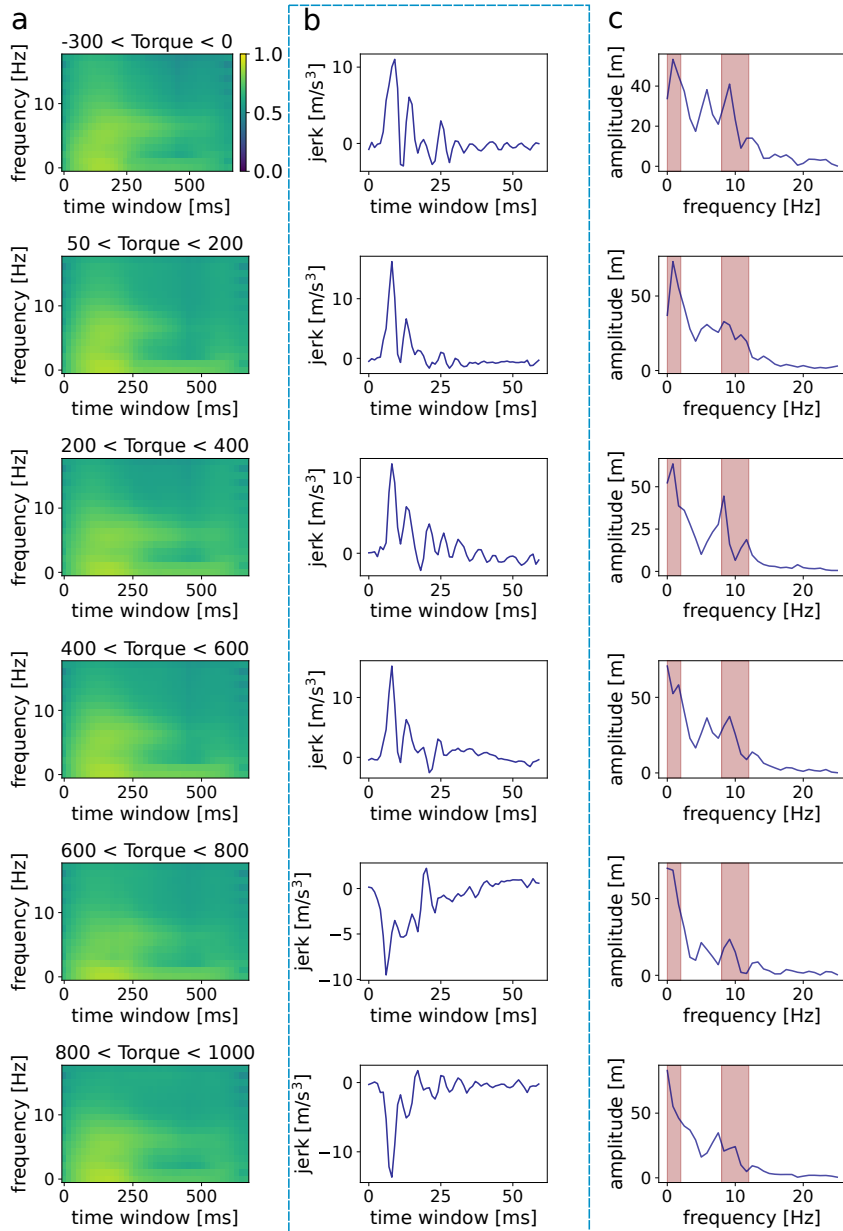


Figure 7: **Unconditional VAE: New jerk signals generation by sampling from the labeled latent space.** **a** Normalized generated spectrograms, **b** generated jerk signals in the time domain, and **c** frequency spectrum of each jerk signal. The shaded areas highlight important frequency bands (0-2 Hz and 8-12 Hz). **Note:** the colorbar displayed in the top subfigure applies to all spectrograms.

spectrograms. The unconditional VAE also shows a higher structural similarity (SSIM = 0.6082) compared to CVAE (SSIM = 0.6051) and GMM-CVAE (SSIM = 0.5759), indicating that it preserves more structural information in the data. Moreover, it outperforms the other models in PSNR (16.7421 dB) and SNR (9.6040 dB), suggesting that it reduces noise more effectively while maintaining signal fidelity. Although CVAE shows comparable performance, it does not provide significant improvements in terms of accuracy. The GMM-CVAE shows higher reconstruction errors and slightly lower SSIM, PSNR,

and SNR, indicating that the additional complexity does not result in better performance in this case. Overall, the unconditional VAE proves to be the most effective model on the testing set for spectrogram reconstruction, capturing the core features of the data while handling noise more effectively than the other VAE variants. While the differences in these spectrogram-domain metrics (like PSNR) between the VAE variants are relatively small, these metrics reflect the direct output of the models. A comparison of generated time-domain jerk signals, also against other modeling approaches, is provided in Section 4.3. However, the CVAEs offer the advantage of conditional generation for specific features like torque demand, which is a key capability for targeted simulations.

The performance metrics for the VAE variants reported in Table 3 are based on a single, fixed random split of the 320 stationary spectrograms into training, validation, and a test set of 32 samples. While this provides a consistent basis for comparison among the VAE models, it is acknowledged that with a test set of this size, the precise metric values might exhibit some sensitivity to different data splits; an exhaustive analysis of this sensitivity (e.g., via cross-validation) was not performed in the current study.

Metric	VAE	CVAE	GMM-CVAE
Average MSE	0.3551	0.3654	0.4055
Average MAE	0.4203	0.4291	0.4652
Normalized MSE	0.3577	0.3681	0.4085
Normalized MAE	0.2969	0.3032	0.3287
Average SSIM	0.6082	0.6051	0.5759
Average SNR (dB)	9.6040	9.5165	9.0451
Average PSNR (dB)	16.7421	16.6546	16.1832

**Table 3: VAEs performance evaluation:** Comparison of performance metrics for the unconditional VAE, CVAE, and GMM-CVAE on the test data set.

We also performed a visual inspection of the original and reconstructed spectrograms and found that CVAE and GMM-CVAE behave very similarly to the unconditional VAE, for which results were reported in Figure 4. Therefore, the corresponding results for CVAE and GMM-CVAE are shown in Appendix B in Figures A1 and A2, respectively.

**Generation of new jerk signals by sampling from the latent space:** Conditional generative models allow the generation of labeled jerk signals for a given torque demand. Figures 8 and A3, the latter included in Appendix B to avoid redundancies here, present new jerk signal generation for a given desired torque demand as a condition using CVAE and GMM-CVAE, respectively. Figures 8a and A3a show a newly generated jerk spectrogram obtained for a specific torque and vehicle type A, for CVAE and GMM-CVAE, respectively. Figures 8b and A3b show the corresponding jerk signal. The corresponding frequencies for the generated signal are shown in Figures 8c and A3c, where the highlighted regions represent the frequencies having the highest amplitudes, i.e., around 0 and 20 Hz. This shows the validity of the generated signal.

As in the unconditional case, Figures 8 and A3 show that the conditional VAEs have effectively learned the underlying distribution of the jerk signals. Unlike the unconditional VAE, which could only generate jerk signals from labeled torque ranges, the conditional VAE allows for generating jerk signals by specifying a precise torque value as a condition. This provides a significant advantage when using the VAE as a replacement in drivetrain simulations, where control over specific input parameters is a desired feature. The generated signals are also physically plausible in the CVAE and GMM-CVAE cases, as the jerk signals in the dataset used for training correspond to frequency regions with the highest amplitudes around 0-2 Hz and 8-12 Hz.

When comparing the jerk signals generated by the CVAE (e.g., Figure 8) with those from the unconditional VAE for similar torque ranges (e.g., Figure 7), some differences in character may be

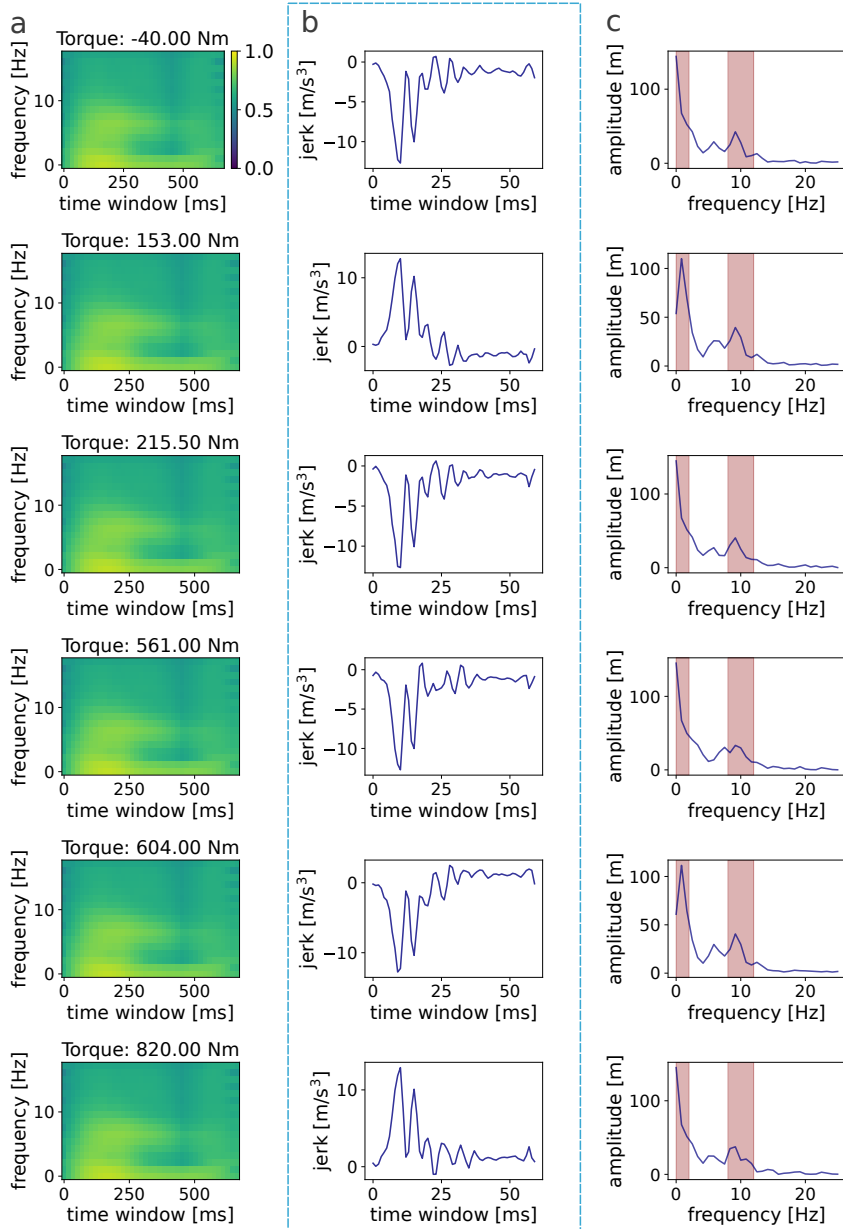


**Figure 8: CVAE: New jerk signals generation by sampling from the latent space given a desired torque demand as condition. a** Generated spectrograms, **b** generated jerk signals in the time domain, and **c** frequency spectrum of each jerk signal. The shaded areas highlight important frequency bands (0-2 Hz and 8-12 Hz). **Note:** the colorbar displayed in the top subfigure applies to all spectrograms.

observed. This can be attributed to the distinct ways the latent spaces are structured and utilized. The unconditional VAE learns a general latent representation, and sampling from visualized torque-range regions taps into this shared space. In contrast, the CVAE's latent space is explicitly conditioned on the torque demand. This conditioning tends to create a more structured latent space where specific torque inputs map to more defined regions, leading to generated signals that are highly consistent with

the given condition, potentially with different diversity characteristics compared to samples from the unconditioned VAE for a broader torque category.

#### 4.3. Comparison between conditional generative-, physics-, and hybrid-based models

In this section, we compare the predictive performance of a physics-based drivetrain model (referred to as physics-based model), a hybrid model, and the CVAE generative model for the dataset presented in Section 4.1. The CVAE was chosen here because it represents the best trade-off between accuracy and versatility among the explored VAE architectures; see Table 3. In particular, the unconditional VAE has the limitation that the generated jerk signal cannot be conditioned to a specific torque value, while the GMM-CVAE does not provide a significant improvement in performance over the CVAE and introduces additional complexity in sampling from the approximated likelihood. We refer the reader to Appendix C for details of the setup of physics-based and hybrid models.

Table 4 summarizes the MSE values for the jerk signals generated by each model. As the physics-based model is a simplified representation (specifically, the two-mass spring-mass oscillator system mentioned in Section 2), it results in a much lower accuracy compared to the data-driven and hybrid approaches. This simplified model serves as a basic benchmark and is not intended to be representative of the sophisticated, highly calibrated physics-based simulation tools used in detailed industrial applications. Its performance underscores the difficulty in achieving high fidelity with basic physical formulations alone and motivates the use of data-driven techniques like VAEs or hybrid models to capture more complex system behaviors. This could be improved by using a more sophisticated physics-based model, which was, however, out of scope for this study. Also note that our goal is to increase the efficiency of the drivetrain development process, and the development of such physics-based models is generally time-consuming.

The hybrid model, which utilizes a 7-million-parameter U-Net convolutional neural network architecture as a data-driven correction stage on top of a basic drivetrain physics simulator (see Appendix C for details), demonstrates slightly better accuracy in predicting time-domain jerk signals than the CVAE when the CVAE is used generatively for a given condition (Table 4). We acknowledge that the U-Net in the hybrid model has significantly more parameters (7 million) compared to our VAE architectures. This notable difference in model scale (roughly a factor of 15-20) means the comparison is not strictly like-for-like in terms of model complexity or data requirements, although the discrepancy is not as large as three orders of magnitude. The primary focus of the VAE development was on generative capabilities and interoperability with more compact models. The U-Net hybrid model is presented here as a benchmark, representing a high-performance approach for signal prediction in this domain, which helps contextualize the CVAE's generative performance. Its substantially higher number of parameters makes it significantly more data-intensive and challenging to train compared to the VAEs tested in this study. This complexity underscores the trade-off between accuracy and model efficiency (referring to aspects like lower data requirements for training, fewer model parameters, and potentially faster inference or training times), with VAEs offering a more practical alternative for scenarios with limited data availability or computational resources. A detailed comparison with hybrid models having a parameter count similar to the VAEs was not performed in this study but could be a direction for future work to assess parameter efficiency more directly for the predictive task.

Metric	Physics-based Model	Hybrid Model	CVAE
MSE	181.2	0.4656	1.9355

Table 4: **Comparison of physics-based model, hybrid, and CVAE as a generative model.** The MSE was computed as the mean squared error between the actual and generated signals (not spectrograms) over the common test set consisting of 32 jerk signals (derived from the stationary signals described in Section 4.1). All models in this table were evaluated on these same 32 test signals to ensure comparability.

## 5. Conclusion

In this study, we showed the potential of deep generative models, specifically VAEs and their conditional variants, for drivetrain simulation. Conventional supervised models map drivetrain behavior based on input settings, but our work introduces a self-supervised approach using VAEs. We demonstrated how VAEs encode jerk signal information into a latent space, enabling the generation of new meaningful jerk scenarios through sampling. Extending this concept, we implemented two conditional VAEs to address simulation tasks that depend on a specific driver torque demand. In particular, we could conclude the following:

- All three VAE versions effectively learn the main features for generating new jerk signals. The unconditional VAE, although unable to generate signals for a specific torque value, produces a latent space that, when projected into two dimensions using t-SNE, shows clearer clustering based on different torque categories. This latent space can be labeled, allowing for the generation of new signals from distinct clusters. On the other hand, both the CVAE and GMM-CVAE show less defined clusters in the latent space but allow for generating jerk signals for specific torque values. The GMM-CVAE does not offer any significant advantage over the CVAE, and both require similar training times ( $\approx 8$  minutes on a personal laptop).
- When measuring the absolute error between original and generated spectrograms, localized errors of up to 25% are observed. Initially, this might suggest poor reconstruction, but a closer look reveals that the original spectrograms appear noisy, whereas the generated ones are smoother. This suggests that the VAE filters out noise and captures the core features. After applying a Gaussian filter to smooth the original spectrograms in an auxiliary analysis, the absolute error between the VAE's reconstruction and these smoothed spectrograms decreased, confirming the VAE's tendency to produce smooth outputs. However, when we trained a VAE model using these artificially smoothed spectrograms as input, the subsequently generated signals sometimes exhibited unexpected frequency peaks, deviating from the dominant 0-2 Hz and 8-12 Hz frequencies typically seen in the original data. Thus, this exploratory experiment suggested that although pre-smoothing the input data can reduce certain reconstruction error metrics, it does not necessarily improve the VAE's generative capability for physically plausible signals from the original noisy distribution and might even hinder it. The VAE's ability to generate meaningful signals from noisy data suggests that it effectively captures the essential features, showing resilience to noise. No significant differences in KL divergence were observed during training when using the original or smoothed spectrograms.

Overall, we conclude that VAEs are a promising alternative to traditional physics-based and hybrid approaches commonly reported in the literature. Our findings position VAEs as a powerful tool for generating realistic jerk signals without prior system knowledge, while conditional VAEs enable the production of torque-specific signals. This has the potential to reduce the need for costly and intensive on-road vehicle testing, underscoring VAEs potential as a valuable tool in electric vehicle modeling and validation.

## Appendix A. Performance metrics to evaluate VAE, CVAE, and GMM-CVAE performance

Several metrics are used to evaluate the model performance, as follows.

**Mean Squared Error (MSE):** MSE measures the average squared difference between the original and reconstructed data. For a batch of spectrograms  $\mathbf{X} = [\mathbf{x}_1, \mathbf{x}_2, \dots, \mathbf{x}_N]$  and their reconstructions  $\hat{\mathbf{X}} = [\hat{\mathbf{x}}_1, \hat{\mathbf{x}}_2, \dots, \hat{\mathbf{x}}_N]$ , the MSE is given by:

$$\text{MSE} = \frac{1}{N} \sum_{i=1}^N \|\mathbf{x}_i - \hat{\mathbf{x}}_i\|^2 \quad (\text{Appendix A.1})$$

where  $N$  is the size of the batch.

**Mean Absolute Error (MAE):** MAE calculates the average absolute difference between the original and reconstructed data. It is defined as:

$$\text{MAE} = \frac{1}{N} \sum_{i=1}^N |\mathbf{X}_i - \hat{\mathbf{X}}_i|. \quad (\text{Appendix A.2})$$

**Normalized MSE (NMSE):** NMSE normalizes the MSE to account for the variance of the spectrogram data, allowing for better comparison across different datasets. It is defined as:

$$\text{Normalized MSE} = \frac{\text{MSE}}{\sigma_X^2} \quad (\text{Appendix A.3})$$

where  $\sigma_X^2$  is the variance of the spectrogram pixel values.

**Normalized MAE (NMAE):** Similarly, the normalized MAE accounts for the mean absolute deviation of the spectrogram data:

$$\text{Normalized MAE} = \frac{\text{MAE}}{\frac{1}{N} \sum_{i=1}^N |\mathbf{X}_i - \mu_X|} \quad (\text{Appendix A.4})$$

where  $\mu_X$  is the mean of the spectrogram pixel values.

**Structural Similarity Index Measure (SSIM):** SSIM measures the structural similarity between the original and reconstructed spectrograms, considering luminance, contrast, and structure. For two signals  $\mathbf{X}_i$  and  $\hat{\mathbf{X}}_i$ , SSIM is given by:

$$\text{SSIM}(\mathbf{X}_i, \hat{\mathbf{X}}_i) = \frac{(2\mu_X\mu_{\hat{X}} + C_1)(2\sigma_{X\hat{X}} + C_2)}{(\mu_X^2 + \mu_{\hat{X}}^2 + C_1)(\sigma_X^2 + \sigma_{\hat{X}}^2 + C_2)} \quad (\text{Appendix A.5})$$

where  $\mu_X$  and  $\mu_{\hat{X}}$  are the means of  $\mathbf{X}_i$  and  $\hat{\mathbf{X}}_i$ ,  $\sigma_X^2$  and  $\sigma_{\hat{X}}^2$  are the variances,  $\sigma_{X\hat{X}}$  is the covariance, and  $C_1, C_2$  are small constants to stabilize the division.

**Signal-to-Noise Ratio (SNR):** SNR is a measure of signal quality, comparing the signal power to the noise power introduced during reconstruction. It is given by:

$$\text{SNR} = 10 \log_{10} \left( \frac{\text{signal power}}{\text{error power}} \right) \quad (\text{Appendix A.6})$$

where:

$$\text{signal power} = \frac{1}{N} \sum_{i=1}^N \mathbf{X}_i^2, \quad \text{error power} = \frac{1}{N} \sum_{i=1}^N (\mathbf{X}_i - \hat{\mathbf{X}}_i)^2 \quad (\text{Appendix A.7})$$

**Peak Signal-to-Noise Ratio (PSNR):** PSNR is used to measure the ratio between the maximum possible signal power and the noise power. It is calculated as:

$$\text{PSNR} = 10 \log_{10} \left( \frac{\text{MAX}^2}{\text{MSE}} \right) \quad (\text{Appendix A.8})$$

where MAX is the maximum pixel value of the original spectrogram, and MSE is the mean squared error between the original and reconstructed spectrograms.

These metrics provide a comprehensive evaluation of the performance of the VAE in terms of reconstruction quality, structural similarity, and noise handling.

## Appendix B. Complementary results for conditional VAEs

Figures A1 and A2 illustrate the performance of conditional VAEs. Figures A1a and A2a compare the original and generated jerk signals in the time domain, showing strong alignment, indicating good reconstruction capability. In Figures A1b and A2b, the original spectrogram is shown, while Figures A1c and A2c show the VAE generated spectrograms, which closely resemble the original. Figures A1d and A2d depict the absolute error between the original and generated spectrograms. As in the unconditional VAE, local discrepancies, observed as pronounced peaks in the absolute error plot, can be attributed to the noise in the original spectrograms, while the VAE tends to reconstruct a smoothed version.

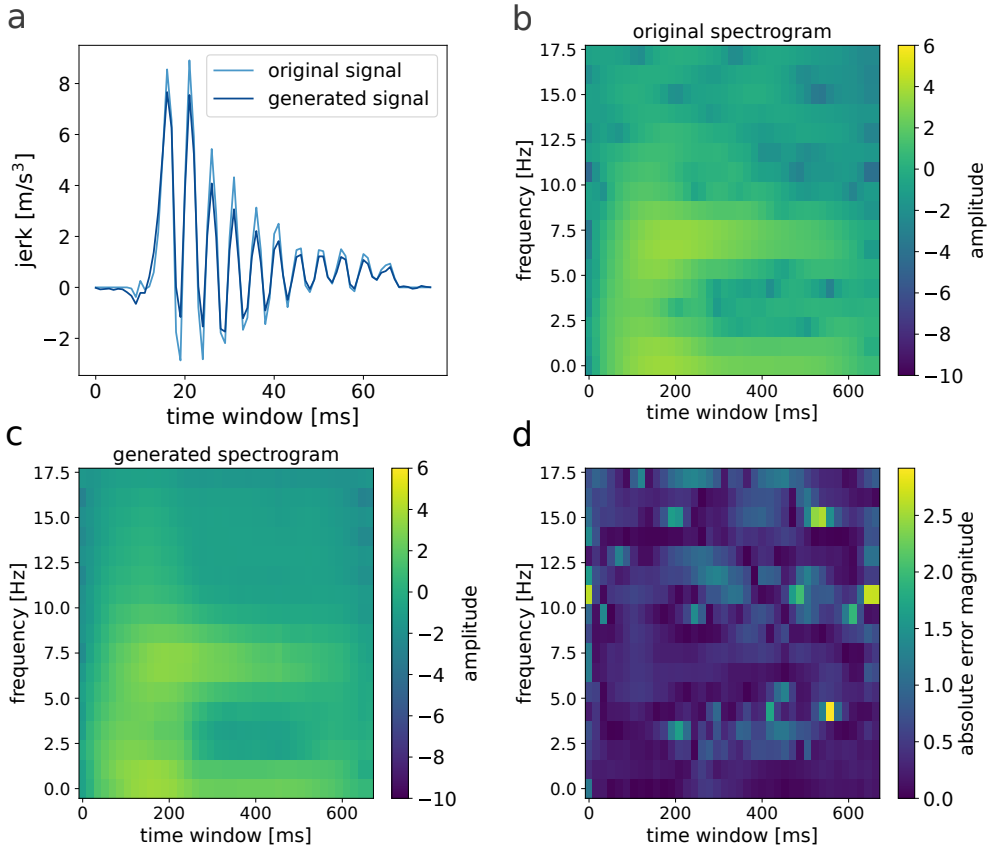


Figure A1: **CVAE:** Model performance evaluation in reconstructing the original spectrogram and jerk signal. **a** Comparison between the original and generated jerk signals in the time domain, **b** original spectrogram, **c** generated spectrogram from the CVAE, and **d** absolute error between the original and generated spectrograms.

Figure A3a shows a newly generated jerk spectrogram obtained for a specific torque and vehicle type A. Figure A3b shows the corresponding jerk signal. The corresponding frequencies for the generated signal are shown in Figure A3c, where the highlighted regions depict the frequencies having the highest amplitudes, i.e., around 0 and 20 Hz. This shows the validity of the generated signal.

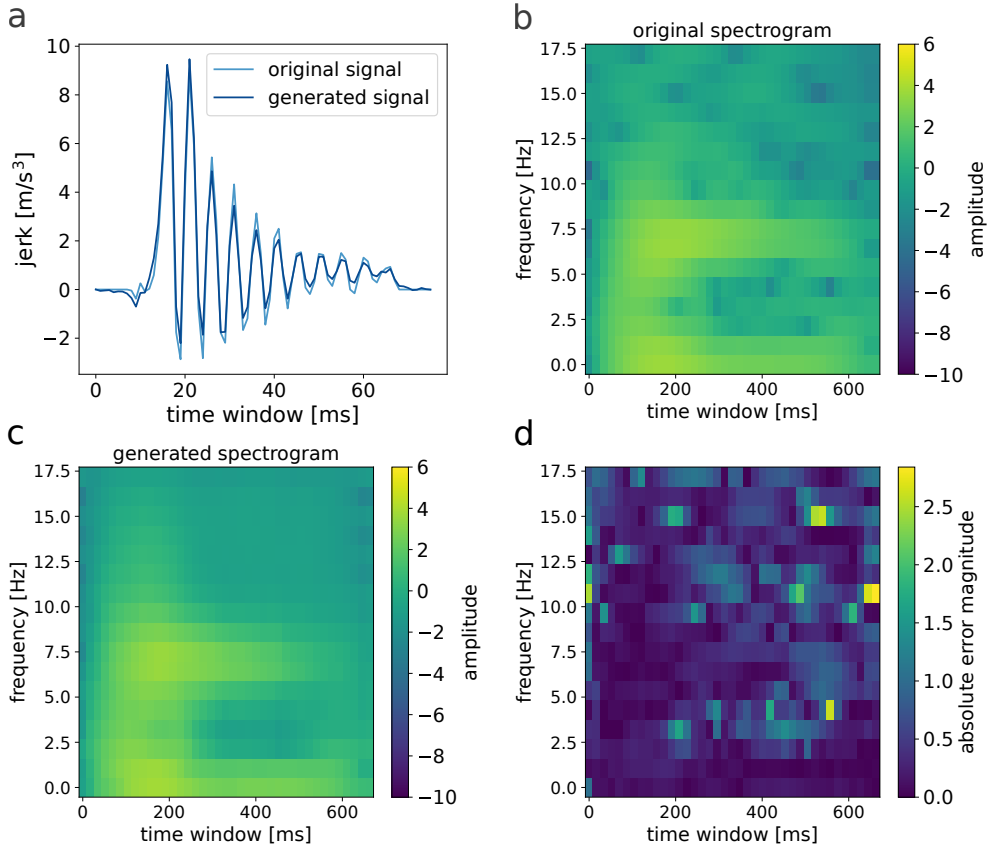


Figure A2: **GMM-CVAE:** Model performance evaluation in reconstructing the original spectrogram and jerk signal. **a** Comparison between the original and generated jerk signals in the time domain, **b** original spectrogram, **c** generated spectrogram from the VAE, and **d** absolute error between the original and generated spectrograms.

### Appendix C. Physics-based and hybrid models set up

To remove the unwanted effect of jerk, one can calibrate the engine maps by building a physics-based hardware simulator that simulates the jerk and acceleration given a torque signal as input. Theoretically, the simulator could create signals close to the real world, but complex physical interactions affect the accuracy of the simulations and cause them to diverge from real measurements. As a consequence, one can build a hybrid hardware simulator by adding a correction model [53, 54, 55]. The correction model is used to bring the simulated signal close to reality by learning complex physical interactions from the data. To do so, a neural network trained on [simulated acceleration; measured acceleration] pairs can be used, as we choose to use the acceleration signal for calibration purposes.

In this work, we use a Matlab Simulink model for our physics-based hardware simulator. The Simulink model implements the basic physics formula to simulate the acceleration signal and takes into consideration hardware parameters such as vehicle mass (kg), gear ratio, inertia rotation ( $\text{kg} \cdot \text{m}^2$ ), stiffness (Nm/degrees), and wheel radius (meters).

Our hybrid simulator approach relies on a correction model on top of a physics-based hardware simulator, and we compare it with the CVAE model. The correction model consists of a neural network (NN) that corrects the simulator output, bridging the gap between simulated and real data.

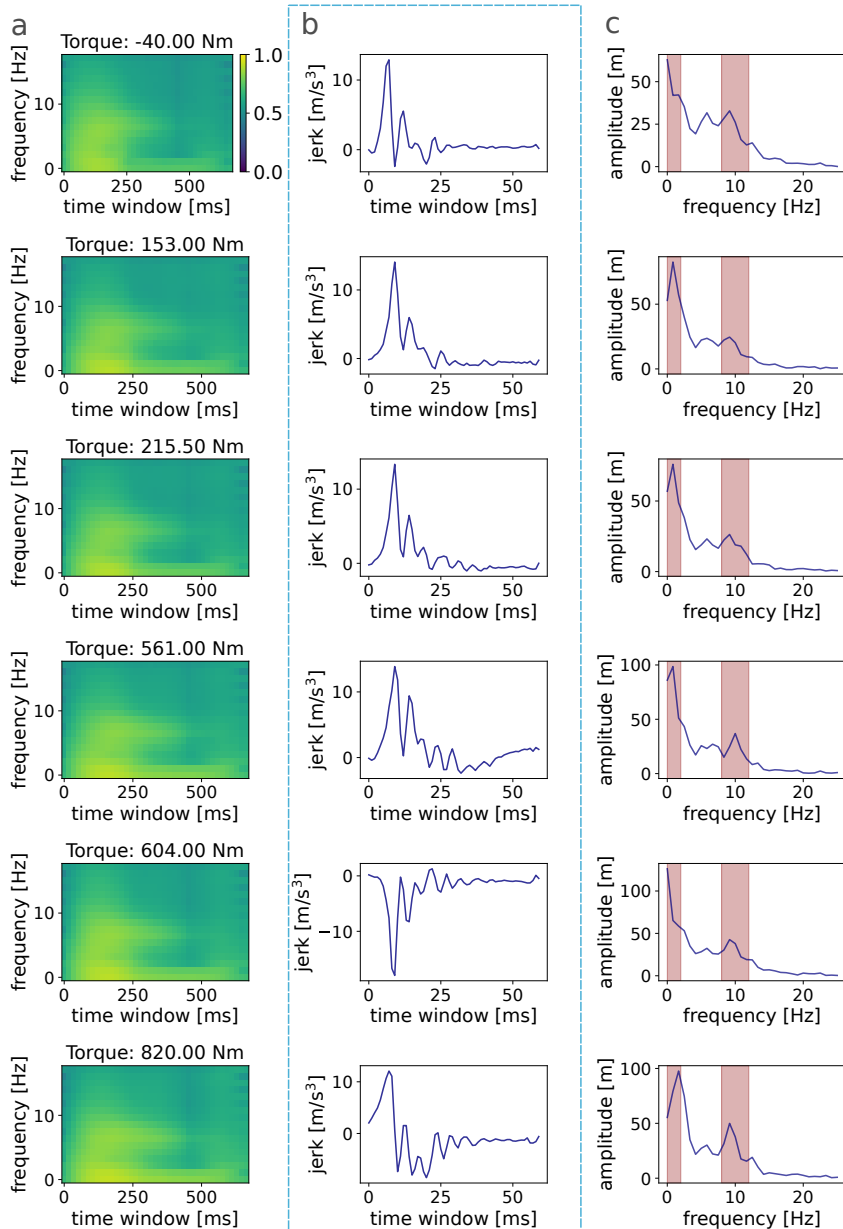


**Figure A3: GMM-CVAE: New jerk signals generation by sampling from the latent space given a desired torque demand as condition.** **a** Generated spectrograms, **b** generated jerk signals in the time domain, and **c** frequency spectrum of each jerk signal. The shaded areas highlight important frequency bands (0-2 Hz and 8-12 Hz). **Note:** the colorbar displayed in the top subfigure applies to all spectrograms.

The input to the NN is composed of 2 channels: the simulated signal (acceleration) and torque demand. There is only one output: the corrected signal that corresponds to the real acceleration. The NN model was trained using data collected from a test bench and real-world measurements.

U-Net is a fully convolutional neural network architecture that evolved from the traditional convolutional neural network and was first designed and applied in 2015 to process biomedical images [56]. It is an encoder-decoder architecture with skip connections (residual connections) between the encoder

and decoder layers. Although originally developed for image data, the U-Net architecture can be applied to signal processing [57]. We chose U-Net as the architecture for our neural network model [56]. The U-Net original design was modified using 1D convolutions with architectural changes inspired by [58]. The main takeaway is that we use the ConvNeXt block [58] with inverted bottleneck [59] as the base convolution block. We use a U-Net with 7 million parameters, a convolution base number of filters equal to 96, and a kernel size of 7.

**Acknowledgments.** The authors acknowledge discussions with David Anton on Bayesian statistics and generative modeling.

**Funding Statement.** This research has been financed by core funding of Porsche and TU Braunschweig.

**Competing Interests.** None

**Data Availability Statement.** The authors will make the data supporting this study available upon reasonable request.

**Ethical Standards.** The research meets all ethical guidelines, including adherence to the legal requirements of the study country.

**Author Contributions.** **Conceptualization:** P.S., H.W., M.S., B.B., AD.C. and L.V.; **Experimental data acquisition:** L.V., M.S. and AD.C. **Software:** P.S., JH.UQ., B.B., AD.C. and L.V.; **Data visualization:** P.S., JH.UQ., B.B. and L.V.; **Formal analysis:** P.S., JH.UQ., B.B., AD.C., H.W. and M.S.; **Writing original draft:** P.S., JH.UQ., AD.C., H.W. and M.S.; **Funding acquisition:** H.W., M.S.; JH.UQ. and B.B. contributed equally as second authors to this work; All authors approved the final submitted draft.

## References

- [1] Xianjian Jin, Guodong Yin, and Nan Chen. Advanced estimation techniques for vehicle system dynamic state: A survey. *Sensors*, 19(19):4289, 2019.
- [2] Feyijimi Adegbohun, Annette Von Jouanne, Ben Phillips, Emmanuel Agamloh, and Alex Yokochi. High performance electric vehicle powertrain modeling, simulation and validation. *Energies*, 14(5):1493, 2021.
- [3] Zhiguo Zhao, Haijun Chen, Jie Yang, Xiaowei Wu, and Zhuoping Yu. Estimation of the vehicle speed in the driving mode for a hybrid electric car based on an unscented Kalman filter. *Proceedings of the Institution of Mechanical Engineers, Part D: Journal of automobile engineering*, 229(4):437–456, 2015.
- [4] Azhaganathan Gurusamy, Bragadeswaran Ashok, and Byron Mason. Prediction of electric vehicle driving range and performance characteristics: A review on analytical modeling strategies with its influential factors and improvisation techniques. *IEEE Access*, 11:131521–131548, 2023.
- [5] Stathi Fotiadis, Mario Lino Valencia, Shunlong Hu, Stef Garasto, Chris D Cantwell, and Anil Anthony Bharath. Disentangled generative models for robust prediction of system dynamics. In *International Conference on Machine Learning*, pages 10222–10248. PMLR, 2023.
- [6] William Gilpin. Generative learning for nonlinear dynamics. *Nature Reviews Physics*, 6(3):194–206, 2024.
- [7] Antoine Caillon and Philippe Esling. Rave: A variational autoencoder for fast and high-quality neural audio synthesis. *arXiv preprint arXiv:2111.05011*, 2021.
- [8] Oscar Pastor-Serrano, Danny Lathouwers, and Zoltán Perkó. A semi-supervised autoencoder framework for joint generation and classification of breathing. *Computer Methods and Programs in Biomedicine*, 209:106312, 2021.
- [9] Diederik P Kingma. Auto-encoding variational bayes. *arXiv preprint arXiv:1312.6114*, 2013.
- [10] Chen Zhang, Riccardo Barbano, and Bangti Jin. Conditional variational autoencoder for learned image reconstruction. *Computation*, 9(11):114, 2021.
- [11] Chunsheng Guo, Jialuo Zhou, Huahua Chen, Na Ying, Jianwu Zhang, and Di Zhou. Variational autoencoder with optimizing Gaussian mixture model priors. *IEEE Access*, 8:43992–44005, 2020.
- [12] Cole Miles, Matthew R Carbone, Erica J Sturm, Deyu Lu, Andreas Weichselbaum, Kipton Barros, and Robert M Konik. Machine learning of Kondo physics using variational autoencoders and symbolic regression. *Physical Review B*, 104(23):235111, 2021.
- [13] Taufique Ahmed and Luca Longo. Latent space interpretation and visualisation for understanding the decisions of convolutional variational autoencoders trained with EEG topographic maps. In *xAI (Late-breaking Work, Demos, Doctoral Consortium)*, pages 65–70, 2023.
- [14] Sabatina Criscuolo, Andrea Apicella, Roberto Prevete, and Luca Longo. Interpreting the latent space of a convolutional variational autoencoder for semi-automated eye blink artefact detection in EEG signals. *Computer Standards & Interfaces*, 92:103897, 2025.
- [15] Andreas Koch, Ludwig Schulz, Gabrielius Jakstas, and Jens Falkenstein. Drivability optimization by reducing oscillation of electric vehicle drivetrains. *World Electric Vehicle Journal*, 11(4):68, 2020.
- [16] Alessandro Scamarcio, Patrick Gruber, Stefano De Pinto, and Aldo Sorniotti. Anti-jerk controllers for automotive applications: A review. *Annual Reviews in Control*, 50:174–189, 2020. ISSN 1367-5788.

- [17] Alessandro Scamarcio, Mathias Metzler, Patrick Gruber, Stefano De Pinto, and Aldo Sorniotti. Comparison of anti-jerk controllers for electric vehicles with on-board motors. *IEEE Transactions on Vehicular Technology*, 69(10):10681–10699, 2020.
- [18] Henrik Schmidt, Kay Büttner, and Günther Prokop. Methods for virtual validation of automotive powertrain systems in terms of vehicle drivability—a systematic literature review. *IEEE Access*, 11:27043–27065, 2023.
- [19] AR Crowther and N Zhang. Torsional finite elements and nonlinear numerical modelling in vehicle powertrain dynamics. *Journal of Sound and Vibration*, 284(3-5):825–849, 2005.
- [20] Xiaohua Zeng, Haoyong Cui, Dafeng Song, Nannan Yang, Tong Liu, Huiyong Chen, Yinshu Wang, and Yulong Lei. Jerk analysis of a power-split hybrid electric vehicle based on a data-driven vehicle dynamics model. *Energies*, 11(6):1537, 2018.
- [21] Yongjun Pan, Xiaobo Nie, Zhixiong Li, and Shuitao Gu. Data-driven vehicle modeling of longitudinal dynamics based on a multibody model and deep neural networks. *Measurement*, 180:109541, 2021.
- [22] Sebastian S James, Sean R Anderson, and Mauro Da Lio. Longitudinal vehicle dynamics: A comparison of physical and data-driven models under large-scale real-world driving conditions. *IEEE Access*, 8:73714–73729, 2020.
- [23] Lekshmi S. and Lal Priya P.S. Mathematical modeling of electric vehicles - a survey. *Control Engineering Practice*, 92: 104138, 2019. ISSN 0967-0661.
- [24] Marius Franck, Jan Philipp Rickwartz, Daniel Butterweck, Martin Nell, and Kay Hameyer. Transient system model for the analysis of structural dynamic interactions of electric drivelines. *Energies*, 14(4), 2021. ISSN 1996-1073.
- [25] Peicheng Shi, Kangji Liu, and Kehang Shi. Integrated design of the torsion beam electric driving axle. *Journal of Vibroengineering*, pages 537–549, jan 2022.
- [26] Prathviraj Shetty and S Dawnee. Modeling and simulation of the complete electric power train of a hybrid electric vehicle. In *2014 Annual International Conference on Emerging Research Areas: Magnetics, Machines and Drives*, pages 1–5. IEEE, 2014.
- [27] D. McDonald. Electric vehicle drive simulation with Matlab/Simulink. In *Proceedings of the 2012 North-Central Section Conference*, pages 1–24, 2012.
- [28] K. L. Butler, M. Ehsani, and P. Kamath. A Matlab-based modeling and simulation package for electric and hybrid electric vehicle design. *IEEE Transactions on Vehicular Technology*, 48(6):1770–1778, 1999.
- [29] R. Zhao, W. Deng, Y. Wang, K. Huang, B. Zheng, and J. Ding. An improved data-driven method for steering feedback torque of driving simulator. *IEEE/ASME Transactions on Mechatronics*, 28(5):2953–2963, Oct. 2023.
- [30] Guohang Li, Miaoqua Huang, Ruiwen Wang, and Wenyuan Zheng. SOH estimation of power battery based on the real vehicle multi-feature and LightGBM algorithm. In *2022 4th International Conference on Frontiers Technology of Information and Computer (ICFTIC)*, pages 511–514, 2022.
- [31] Litao Zhou, Yang Zhao, Da Li, and Zhenpo Wang. State-of-health estimation for lifepo4 battery system on real-world electric vehicles considering aging stage. *IEEE Transactions on Transportation Electrification*, 8(2):1724–1733, 2022.
- [32] Shuwen Sun, Lihong Feng, and Peter Benner. Data-augmented predictive deep neural network: Enhancing the extrapolation capabilities of non-intrusive surrogate models. *arXiv preprint arXiv:2410.13376*, 2024.
- [33] M. Raissi, P. Perdikaris, and G.E. Karniadakis. Physics-informed neural networks: A deep learning framework for solving forward and inverse problems involving nonlinear partial differential equations. *Journal of Computational Physics*, 378: 686–707, 2019. ISSN 0021-9991.
- [34] Katiana Kontolati, Somdatta Goswami, George Em Karniadakis, and Michael D Shields. Learning nonlinear operators in latent spaces for real-time predictions of complex dynamics in physical systems. *Nature Communications*, 15(1):5101, 2024.
- [35] Zheyuan Hu, Nazanin Ahmadi Daryakenari, Qianli Shen, Kenji Kawaguchi, and George Em Karniadakis. State-space models are accurate and efficient neural operators for dynamical systems. *arXiv preprint arXiv:2409.03231*, 2024.
- [36] Jinjiang Wang, Yilin Li, Robert X Gao, and Fengli Zhang. Hybrid physics-based and data-driven models for smart manufacturing: Modelling, simulation, and explainability. *Journal of Manufacturing Systems*, 63:381–391, 2022.
- [37] Sathish Kasilingam, Ruoyu Yang, Shubhendu Kumar Singh, Mojtaba A Farahani, Rahul Rai, and Thorsten Wuest. Physics-based and data-driven hybrid modeling in manufacturing: a review. *Production & Manufacturing Research*, 12(1):2305358, 2024.
- [38] Parth Shah, Silabratra Pahari, Raj Bhavsar, and Joseph Sang-II Kwon. Hybrid modeling of first-principles and machine learning: A step-by-step tutorial review for practical implementation. *Computers & Chemical Engineering*, page 108926, 2024.
- [39] M. Skull, M. Bach, T. Roulet, and M. Hauss. AI-based methodology for the calibration of anti-jerk control on electric drives. *ATZ - Automobiltechnische Zeitschrift*, April 2024.
- [40] D. Griffin and J. Lim. Signal estimation from modified short-time Fourier transform. *IEEE Transactions on Acoustics, Speech, and Signal Processing*, 32(2):236–243, April 1984.
- [41] Alan V Oppenheim. *Discrete-time signal processing*. Pearson Education India, 1999.
- [42] Adam Paszke, Sam Gross, Francisco Massa, Adam Lerer, James Bradbury, Gregory Chanan, Trevor Killeen, Zeming Lin, Natalia Gimelshein, Luca Antiga, et al. Pytorch: An imperative style, high-performance deep learning library. *Advances in neural information processing systems*, 32, 2019.
- [43] GM Harshvardhan, Mahendra Kumar Gourisaria, Manjusha Pandey, and Siddharth Swarup Rautaray. A comprehensive survey and analysis of generative models in machine learning. *Computer Science Review*, 38:100285, 2020.
- [44] Carl Doersch. Tutorial on variational autoencoders. *arXiv preprint arXiv:1606.05908*, 2016.

- [45] Diederik P. Kingma and Max Welling. An introduction to variational autoencoders. *Foundations and Trends® in Machine Learning*, 12(4):307–392, 2019. ISSN 1935-8245.
- [46] R. Mushtaq. Augmented Dickey Fuller test. SSRN, 2011.
- [47] P. Kokoszka and G. Young. KPSS test for functional time series. *Statistics*, 50(5):957–973, 2016.
- [48] Skipper Seabold and Josef Perktold. Statsmodels: econometric and statistical modeling with python. *SciPy*, 7(1), 2010.
- [49] T Tony Cai and Rong Ma. Theoretical foundations of t-SNE for visualizing high-dimensional clustered data. *Journal of Machine Learning Research*, 23(301):1–54, 2022.
- [50] Laurens Van der Maaten and Geoffrey Hinton. Visualizing data using t-SNE. *Journal of machine learning research*, 9(11), 2008.
- [51] Sam Roweis, Geoffrey Hinton, and Ruslan Salakhutdinov. Neighbourhood component analysis. *Adv. Neural Inf. Process. Syst. (NIPS)*, 17(513-520):4, 2004.
- [52] F. Pedregosa, G. Varoquaux, A. Gramfort, V. Michel, B. Thirion, O. Grisel, M. Blondel, P. Prettenhofer, R. Weiss, V. Dubourg, J. Vanderplas, A. Passos, D. Cournapeau, M. Brucher, M. Perrot, and E. Duchesnay. Scikit-learn: Machine learning in Python. *Journal of Machine Learning Research*, 12:2825–2830, 2011.
- [53] Stefanie Winkler, Andreas Körner, and Felix Breitenecker. Modelling framework for artificial hybrid dynamical systems. *Nonlinear Analysis: Hybrid Systems*, 42:101072, 2021. ISSN 1751-570X.
- [54] John Harlim, Shixiao W. Jiang, Senwei Liang, and Haizhao Yang. Machine learning for prediction with missing dynamics. *Journal of Computational Physics*, 428:109922, 2021. ISSN 0021-9991.
- [55] Matthias Kötter, B. Lindemann, D. Bergmann, M. Ehrly, T. Jung, M. Nijls, S. Thewes, T. Körfer, S. Trampert, T. Drecq, and P. Gautier. Powertrain calibration based on x-in-theloop: Virtualization in the vehicle development process. In *18. Internationales Stuttgarter Symposium*, pages 1187–1201, Wiesbaden, 2018. Springer Fachmedien Wiesbaden.
- [56] Olaf Ronneberger, Philipp Fischer, and Thomas Brox. U-net: Convolutional networks for biomedical image segmentation. *Medical Image Computing and Computer-Assisted Intervention (MICCAI)*, 2015.
- [57] Daniel Stoller, Sebastian Ewert, and Simon Dixon. Wave-U-Net: A multi-scale neural network for end-to-end audio source separation. In *Proceedings of the 19th ISMIR Conference*, 2018.
- [58] Zhuang Liu, Hanzi Mao, Chao-Yuan Wu, Christoph Feichtenhofer, Trevor Darrell, and Saining Xie. A convnet for the 2020s. In *2022 IEEE/CVF Conference on Computer Vision and Pattern Recognition (CVPR)*, 2022.
- [59] Mark Sandler, Andrew Howard, Menglong Zhu, Andrey Zhmoginov, and Liang-Chieh Chen. Mobilenetv2: Inverted residuals and linear bottlenecks. In *Proceedings of the IEEE conference on computer vision and pattern recognition*, pages 4510–4520, 2018.